BRNO UNIVERSITY OF TECHNOLOGY

VYSOKÉ UČENÍ TECHNICKÉ V BRNĚ

CENTRAL EUROPEAN INSTITUTE OF TECHNOLOGY BUT

STŘEDOEVROPSKÝ TECHNOLOGICKÝ INSTITUT VUT

QUANTITATIVE 3D CHARACTERIZATION OF BIOLOGICAL STRUCTURES BY X-RAY COMPUTED MICROTOMOGRAPHY

KVANTITATIVNÍ 3D CHARAKTERIZACE BIOLOGICKÝCH STRUKTUR POMOCÍ RENTGENOVÉ POČÍTAČOVÉ MIKROTOMOGRAFIE

DOCTORAL THESIS SUMMARY

TEZE DIZERTAČNÍ PRÁCE

AUTHOR AUTOR PRÁCE	**Ing. Markéta Tesařová**
SUPERVISOR ŠKOLITEL	**doc. Ing. Tomáš Zikmund, Ph.D.**

BRNO 2022

Summary

Modern developmental biology uses a broad spectrum of methods for analysing structures of interest. Multidisciplinary teams are currently pushing forward the understanding of biological questions using 3D approaches. However, one major challenge of 3D imaging techniques in biology is a lack of methodology for quantifying observed phenomena that are often the cause of developmental or genetic disorders. One of the methods whose application has been widely spread in recent years is X-ray computed microtomography (microCT). This technique provides isotropic resolution up to 1 µm and, when a sample is appropriately prepared, a wide variety of tissue differentiation. However, biological structures are usually diverse in size and shape, and every task requires a specific solution regarding data processing. This work addresses the implementation of microCT for imaging and mainly 3D characterization of biological structures *ex-vivo*. Particular emphasis is given to analysing soft tissues in mouse embryos' heads and imaging salamander species, focusing on their regeneration ability. This work describes the relevant information for microCT users dealing with biological samples; it includes the preparation of the sample for measurements, selecting suitable parameters for the experiment and mainly subsequent quantitative analysis of 3D datasets. The latest technological advancements in 3D imaging were studied and tested on concrete projects in the field of developmental biology, where 3D information from microCT played a key role.

Abstrakt

Moderní vývojová biologie využívá široké spektrum metod k analyzování studovaných struktur. Multioborové týmy v poslední době prosazují využívání 3D přístupu k porozumění biologickým procesům. Jedna z hlavních překážek při využívání 3D zobrazovacích technik v biologii je nedostatek metodologie pro kvantifikování pozorovaných jevů, které často bývají příčinou vývojových či genetických onemocnění. V posledních letech se v biologických výzkumech rozšířilo využití rentgenové počítačové mikrotomografie (mikroCT). Technika mikroCT dokáže poskytnout izotropní rozlišení až 1 µm a při správné přípravě vzorku širokou škálu tkáňové diferenciace. Biologické struktury jsou však rozmanitých velikostí a tvarů a každá struktura vyžaduje specifický přístup v oblasti zpracování dat. Tato práce se zabývá využitím mikroCT pro zobrazování, ale především 3D charakterizaci biologických struktur *ex-vivo*. Zvláštní důraz je kladen na analýzu měkkých tkání v hlavách myších embryí a zobrazování různých druhů mloků se zaměřením na jejich regenerační schopnosti. Tato práce popisuje relevantní informace pro uživatele mikroCT zabývajícími se biologickými projekty: To zahrnuje přípravu vzorku pro měření, výběr vhodných parametrů k samotnému měření, a především analýzu vzniklého 3D datasetu. Nejnovější technologické pokroky ve 3D zobrazovaní byly studovány a testovány na konkrétních projektech vývojové biologie, kde 3D informace získaná pomocí mikroCT hrála klíčovou roli.

Keywords

X-ray computed microtomography, microCT, CT, 3D imaging, biology, mouse embryos, salamanders

Klíčová slova

rentgenová počítačová mikrotomografie, mikroCT, CT, 3D zobrazování, biologie, myší embrya, mloci

TESAŘOVÁ, Markéta. *Quantitative 3D characterization of biological structures by X-ray computed microtomography.* Brno, 2022. Doctoral Thesis Summary. Vysoké učení technické v Brně, Středoevropský technologický institut VUT, Central European Institute of Technology BUT. Supervisor Tomáš Zikmund.

Table of Contents

1 Aims of Doctoral Thesis 2
  1.1 MicroCT measurement and data segmentation of biological samples 2
  1.2 Quantification of segmented 3D models 2
  1.3 Implementation of the results to particular biological projects 2
2 Methods 3
  2.1 Sample preparation 3
  2.2 MicroCT 4
    2.2.1 Laboratory measurements 4
    2.2.2 Synchrotron measurements 5
  2.3 Data analysis 5
3 Results 7
  3.1 Regeneration of salamander limbs 7
  3.2 3D-cell distribution in the regenerative muscle-skeletal system 9
    3.2.1 Number and density of cells within the extracellular matrix 10
    3.2.2 The polarity of the cells in 3D 12
    3.2.3 Joint formation 14
  3.3 Adaptation of Proteus anguinus to dark habitats 15
  3.4 Vertebrate cartilage growth studied on mouse embryos 17
    3.4.1 Wall thickness analysis 20
    3.4.2 Shape comparison 20
    3.4.3 Modelling of cell division based on microCT models 22
  3.5 Extraocular muscles development 22
    3.5.1 Ventralization of the eyeball 23
4 Combination of microCT with other methods 27
  4.1 Neck muscles and associated connective tissues 27
5 Conclusion 30
6 References 31
7 Author publications and other outputs 35
  7.1 Publications 35
  7.2 Products 37
  7.3 Grants 37
  7.4 Conferences 37

Introduction

3D imaging approaches based on CT have become increasingly accessible with technological advancements. The synergy of material and life sciences has impacted industrial and scientific research with new tools for investigation. Multi-disciplinary collectives composed of clinical doctors, biologists, engineers and imaging experts are pushing forward the use of 3D approaches to understanding biological questions. However, one major challenge of 3D techniques in biology is a lack of methodology for quantifying observed phenomena. Biological structures are usually diverse in size and shape, and every task requires a specific solution.

This dissertation work addresses the implementation of X-ray computed microtomography (microCT) for imaging and mainly 3D characterization of biological structures. Particular emphasis is given to challenges that arise with the measurement of biological samples that are not typical for material sciences. Furthermore, the work is written so that students and scientists who want to use microCT for biological projects could take this work as the manual for the complete procedure, starting with preparing samples and ending with the 3D analysis of measured data.

X-ray computed tomography (CT) is a 3D imaging method that can provide information about the internal structures non-destructively from the metres down to micrometres length scales. The first chapter starts with a literature review and introduces the microCT technique by explaining its principles and technological setup. This chapter also addresses the preparation of biological samples for microCT measurement. Data analysis and segmentation are also discussed.

The second chapter defines the dissertation work aims, and the third chapter describes the methodology used. It includes a complete pipeline starting with sample preparation, parameters of microCT measurement and data processing.

The main part of this thesis can be found in the fourth chapter. Each section is dedicated to one specific biological project. The motivation for using the microCT method is given and detailed procedure and analysis are explained. Sections refer to published manuscripts that originated from the presented work and can be found in the appendix of the thesis.

The fifth chapter then focuses on combining microCT with other imaging methods. It describes the motivation for why different techniques were needed, so it naturally defines the capability of microCT imaging. Specifically, it explains the combination of microCT with classical microscopy and histological staining on an example of muscle imaging and connective tissues.

The appendix of the thesis contains a list of author outputs – publications, products, conferences and grants associated with this dissertation work. First-author and co-author publications can be then found in the attachment.

1 Aims of Doctoral Thesis

Even though microCT imaging has made significant progress in biological imaging in the last few years, many challenges still need to be addressed. The main aim of this dissertation is to bring new insight into microCT imaging and mainly subsequent 3D analysis of biological structures. As described below, the thesis aims can be divided into three parts: MicroCT measurement and data segmentation of biological samples, quantification of segmented 3D models and implementation of the results to particular biological projects.

1.1 MicroCT measurement and data segmentation of biological samples

There are three basic approaches for imaging biological samples by microCT: Staining, phase-contrast imaging, dual CT or a combination of these methods. Staining by chemical substances is often used because of the tissues' very similar attenuation coefficient. However, the staining has some limitations: generally, it is usually applied only on ex-vivo samples; shrinking tissue can appear with a longer staining time [1]; penetration of stains is limited etc. [2, 3]. In some cases, phase-contrast imaging is more convenient. The combination of staining and phase-contrast can give a good differential contrast and a higher resolution [4-6]. After getting the 3D dataset, data analysis and segmentation is another challenging task. Because of the complex structures of biological samples, it is hard to find a universal algorithm for the segmentation of biological data. Above that, the staining of soft tissues gives the same greyscale value to various tissue types. Thus, it is challenging to segment data into anatomical structures using conventional segmentation methods. On the other hand, due to the staining, a large variety of tissue can be observed by the human eye. Therefore, manual segmentation is taken as a golden standard [7]. However, this approach can be time-consuming and suffers from operator variability [8].

Therefore, this dissertation aims to set the appropriate strategy for microCT measurement of soft tissues, segment the structures and create a database of segmented data. Then, this database would serve as an input for machine learning algorithms, specifically convolutional neural networks (CNN).

1.2 Quantification of segmented 3D models

To answer the question of biological issues and to reveal and describe complex phenomena, visualization is usually not enough. Developmental studies in biology require the exact number of comparisons of groups with different ages, treatments, or mutations of the samples. Thus, this work should focus on finding ways to quantify differences among different developmental stages or how to compare wild types and mutants quantitatively.

1.3 Implementation of the results to particular biological projects

The main aim of this work is to implement obtained results in practical biological projects with an impact on the biological community. Particular attention should be given to soft tissues that have not been analysed by microCT before, like cartilaginous chondrocranium in mouse embryos, muscles with attachment points, tendons, and supportive tissues with a focus on their developmental programs. The dissertation work should also interactively reflect the needs of biologists for the segmentation and quantification of the studied structures.

2 Methods

All animal work (mouse embryos and salamanders) was approved and permitted by the Ethical Committee on Animal Experiments (Norra Djurförsöksetiska Nämnd) and conducted according to the Swedish Animal Agency's Provisions, and Guidelines for Animal Experimentation and international guidelines and regulations were followed (Institutional Review Board/Institutional Animal Care and Use Committee). Mouse embryos for extraocular muscles project and investigation of neck muscles were handled as per European Community guidelines, and the ethics committee of the Institut Pasteur (CTEA) approved protocols (APAFIS#6354–20160809 l2028839).

2.1 Sample preparation

Staining with elements with higher atomic numbers turned out to increase the contrast of the soft tissues as the best option. Several staining protocols were tested to visualize mouse brain structures by microCT. Samples were stained in PTA, iodine or a combination of both solutions for various periods [1]. The staining protocols were modified by the work of Metscher [2, 3]. In summary, the staining in iodine exhibited more clear contours of fibres than in the case of PTA-stained samples. Fixation of samples in 4% PFA demonstrated higher contrast to tissues fixed in 10% PFA. Also, when iodine is compared to PTA, PTA appears as a larger molecule with much slower tissue penetration rates [2].

The staining time depends on the size of the sample. For samples larger than a few millimetres (i.e. mouse embryos 17.5 days post fertilisation and older), PTA penetration to the samples is limited. To improve the penetration of staining agents to the sample, we applied a few small holes by the needle to the skin of the sample (see Fig. 2.1). However, it turned out that they don't serve as the input for staining the whole sample. Another attempt was to cut to some parts to fasten the staining. The dissected area had faster perfusion of contrasting agents and decreased the staining time. However, the staining of PTA was still very slow and limited, and the sample did not stay intact. By applying iodine, it has turned out that staining time decreased significantly (from weeks with PTA to days with iodine, depending on the size of the sample). Both, the PTA and iodine stains were found to impart strong tissue contrast to soft tissues [2]. On the example of mouse embryo, soft tissues are stained almost equally, and they give similar input for segmentation, both manual and semi-automatic. A more detailed comparison of iodine and PTA staining with different concentrations and staining times can be found in the attached manuscript [1].

The next step after staining the sample is the sample's fixation for microCT measurement. Mechanical stability (both the CT machine and the specimen) is essential for high data quality. The motions must be smaller than the voxel size; otherwise, the reconstructed 3D volume will be blurred, as shown in Fig. 2.2. Biological samples were placed in polyimide/capton tubes filled with 1% agarose gel to ensure stability.

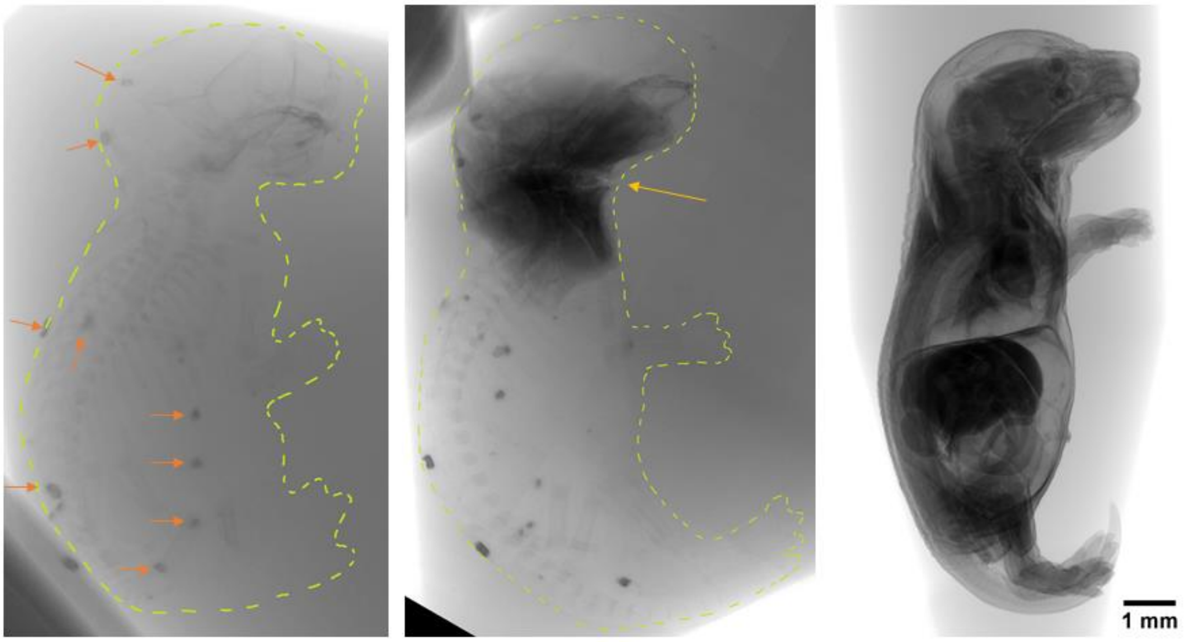

PTA staining: Small holes by needle PTA staining: Cut in the neck area Iodine staining

Figure 2.1: Problems of staining by PTA for samples larger than a few millimetres. The left image shows an improperly stained mouse embryo with holes by needle – only the areas of the needle marks (orange arrows absorbed some of the contrasting agents, but staining didn't penetrate to the sample. The middle image shows the cut in the neck area (yellow arrow). The right image shows staining by iodine instead of problematic PTA.

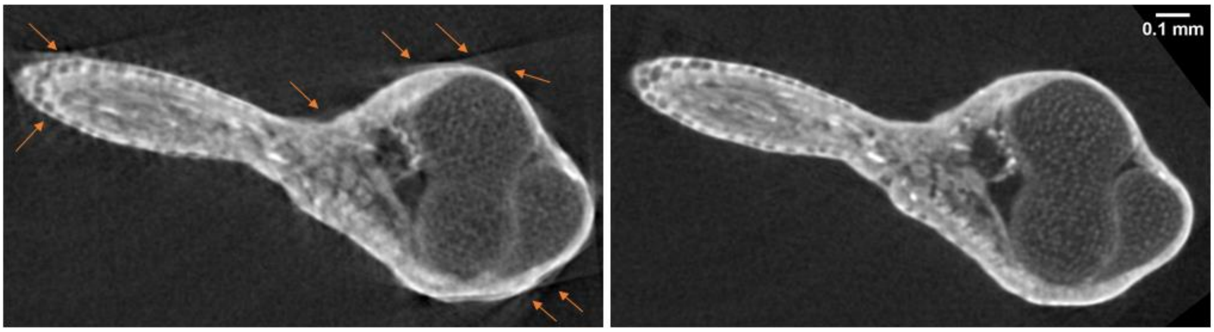

Figure 2.2: Artefacts caused by movement of the sample during microCT measurement in the reconstructed CT slices of a salamander limb. Orange arrows show blurred areas in the CT slice.

2.2 MicroCT

2.2.1 Laboratory measurements

CT measurements on laboratory equipment were realized in the laboratory of X-ray micro and nanocomputed tomography at CEITEC BUT in Brno. MicroCT machine GE phoenix v|tome|x L 240 is equipped with a 180 kV/15W maximum power nanofocus X-ray tube and high flat-panel dynamic 41|100 with 4000 × 4000 pixels and a pixel size of 100 × 100 µm.

The first step was to find suitable parameters for microCT measurement. It means to find proper sample-source and source-detector distance and find X-ray tube parameters for sufficient contrast. Because the illumination provided by X-ray sources is not uniform, and detectors show pixel to pixel variations in sensitivity, a projection must be acquired without the sample between source and detector. A bright, featureless image is captured to normalize the optical defects. The projection must be collected under the same conditions as the CT scan (i.e. same source-detector distance and parameters of the X-ray tube). This process compensates for these variations and is called a flat field correction [9].

As described in the previous section, mechanical stability is essential for microCT measurement. At the same time, the stability of the sample is ensured by putting the sample in agarose gel. Furthermore, the mechanical stability of the system is secured by granite slabs that dampen vibration that could affect the fluency of rotation of the sample during microCT scanning. Anyway, there is always some motion except the rotation of the sample during the scanning. To compensate for this motion, GE phoenix v|tome|x L 240 has a module that manages to compensate for a slight movement called scan|optimizer. The projections acquired at 0° and 360° should be identical. Scan|optimizer captures several X-ray images from different angles before the measurement. The module compares the images captured before and during the measurement at appropriate angles to ascertain whether there has been any movement during tomographic measurement. If there is a motion, the module can compensate for it during the reconstruction.

Information about applied acceleration voltage, current, exposure time, and the number of projections and filters for each sample are specified in publications that originated from the doctoral thesis. The voxel size of obtained volumes was in the range of 1 µm for samples in the range of a few mm to 10-20 µm for samples in the range of a few cm.

2.2.2 Synchrotron measurements

Synchrotron experiments were conducted at Sincrotrone Elettra in Italy under the supervision of Dr. Lucia Mancini. Measurements were held at SYRMEP (Synchrotron Radiation for Medical Physics) beamline using the white beam radiation mode. The samples were fixed in 1% agarose gel in polyimide or plastic tubes. During the first measurements, some motion artefacts occurred. Tiny bubbles were found in agarose gel, probably created by overheating the samples. Also, a change in the colour to blue was observed. Thus, we optimized scanning parameters to reduce the scanning time. After optimization, we decreased from the original 40 minutes to 17 minutes per scan: Exposure time was 1.0 s per projection, with 1000 projections acquired over a total scan angle of 180°. The X-ray spectrum of the beam was filtered with 1.5 mm of silicon and 0.025 mm of molybdenum. The sample-detector distance was set at 100 mm. The first set of experiments was realized with a voxel resolution of 2.5 µm, and according to the size of the sample, it was tuned up to 1 µm. The tomographic slices were reconstructed using the SYRMEP Tomo Project (STP) software. The phase retrieval algorithm was implemented in STP software, which became crucial for visualising cells. Details of the synchrotron experiment realized on salamander limbs can be found in [4].

2.3 Data analysis

Tomographic data from GE phoenix v|tome|x L 240 were reconstructed with GE phoenix datos |x 2.0 3D computed tomography software (Waygate Technologies GmbH Germany). A scan optimiser module was applied during the reconstruction as described in the previous section regarding laboratory measurement to compensate for the small and smooth drift of the axis (samples and detector) and focus (X-ray tube) position. The output of the reconstructed CT slices was a 16-bit integer. For manual segmentation, 3D datasets were transformed to 8bit DICOM format to save processing time and reduce the size of the data to save space on the disk. Segmentation of structures was performed using software Avizo and VG Studio Max (Volume Graphics GmbH, Germany) as described in [8]. Firstly, the structures of interest were outlined in every 3rd to 5th slice manually or semi-automatically using watershed segmentation. Then, the mask was interpolated between slices. Segmentation along one direction caused disfluencies in the perpendicular direction.

For this reason, the segmented masks were transformed into STL model and smoothed in VG Studio MAX software. The smoothing was controlled to preserve the small details in the original data. Quantitative analyses on the segmented structures were performed in VG Studio MAX software.

Another challenge of microCT imaging is effectively and intuitively sharing complex datasets between scientists from different fields. Generally, 3D datasets need special software for visualisation or are reduced to 2D images in which important information might be lost. For this reason, we created a manual that describes individual steps for creating an interactive 3D PDF file allowing rotation, movement or magnification to provide an intuitive approach to analysing structures in a 3D context. This manual is widely applicable in biological research and can be used to analyse volumetric data from any research field relying on 3D rendering and CT-biomedical imaging [10].

This manual can be found in the attachments of this document and was published as supplementary material in my work about interactive and intuitive visualisation methods for 3D data [10]. It contains a detailed description of the pipeline to create a personalised interactive 3D PDF file. Our procedure involves a combination of free (Meshlab, Blender) and commercial (Avizo, VG Studio, 3D PDF Maker) software. Alternatively, segmentation or remeshing of the model can be done with other appropriate software [10].

3 Results

3.1 Regeneration of salamander limbs

Knowing the principles and limitations of regeneration is necessary for controlling the opportunity to restore damaged tissues or organs. While humans show poor regenerative ability, other vertebrates can regenerate diverse body structures. Salamanders exhibit the most remarkable regenerative ability among amphibians. They can regrow ocular tissues, nervous system, whole body parts and organs such as the heart [11]. Such conservation of regenerative principles gives hope to applying the basic knowledge obtained in salamanders to human regeneration in the distant future. Limb regeneration in salamanders is a well-established model system [11]. The speed of salamander limb regeneration varies among species and developmental stages, and they can regenerate entire limbs in a range of days to weeks. [12].

Regeneration is often interpreted as a repetition of embryonic development. It is believed that a regenerated limb is an entirely normal anatomical and functional limb. However, whether each regenerated limb is really an unequivocal copy has not been confirmed. Regeneration results in a limb of the same size; however, the regeneration process is not perfect, and the patterning defects and anomalies have been documented in regenerated limbs [13]. Certainly, developmental mechanisms play an essential role during regeneration. However, structures have much larger size and speed of growth together with environmental conditions in a regenerating limb are different. To question the exactness of the regenerative process, we focused on *Ambystoma mexicanum* (also known as axolotl) and *Pleurodeles waltl*. We used the microCT technique to trace the transformation of the blastema to the new limb by scanning the salamander limb in the different stages after amputations to compare developmental and regenerative formation mechanisms. Already three weeks after amputation, we observed cartilage in the regenerating limb. Every week, a limb was collected, and a 3D model was created. Thus, we were able to follow the regeneration process in time.

In fully regenerated limbs, we also looked at the process of ossification. It was challenging to find and segment ossified cartilage and newly formed bone in microCT data. Developing and regenerating limbs undergo different ossification types. To segment cartilage, the semi-automatically method worked as cartilage is stained significantly weaker than surrounding tissue [8]. However, mineralized bone has higher X-ray attenuation and appears in lighter areas. Stained muscles also show higher attenuation with similar contrast to the bone. Above that, muscles touch the bone and thus, it is hard to find the border of the bone automatically. Therefore, special attention was given to these areas. In another step, bone and cartilage were separated based on their greyscale value (Fig. 3.1).

When having a 3D model of cartilage and bone, we looked at the shape of segmented structures in more detail. When looking at the segmented models, it seemed that regenerated limbs have thicker cartilage and bone, respectively, compared to control limbs undergoing normal development. Firstly, to confirm this hypothesis, I divided the 3D model of all segmented elements into sub-models. The anatomically corresponding parts were taken into the same coordinate system in the second step. By changing the opacity of the registered models, it became clear that the length of the models is comparable.

On the other hand, the thickness of regenerated elements is thicker. To gain some quantitative numbers for confirmation of this observation, nominal/actual comparison analysis in VG studio software was performed. This type of analysis was developed to compare two mesh models. The parts of the models with the same position are shown in green colour. When a deviation occurs, the distance between the meshes is computed and then demonstrated by colour-coding on the model. The whole process of shape comparison is shown in Fig. 3.2.

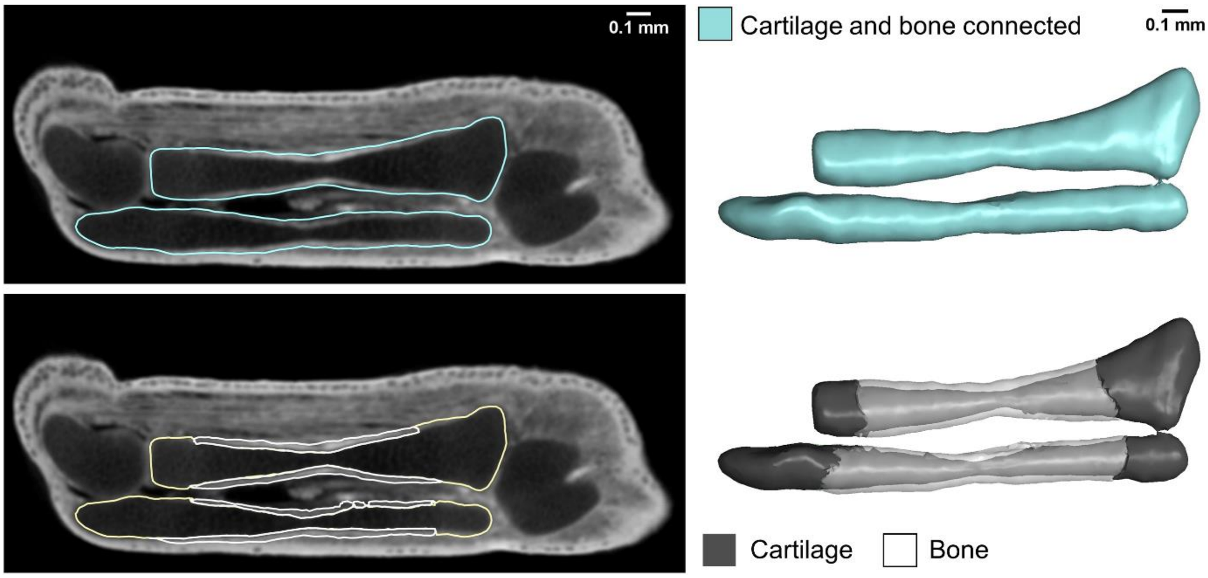

Figure 3.1: Semi-automatic segmentation of bone and cartilage in *ulna* and *radius* in salamander limb. The top image shows the segmentation of skeletal elements as one 3D model. The bottom image shows separated models for bone and cartilage based on their greyscale value.

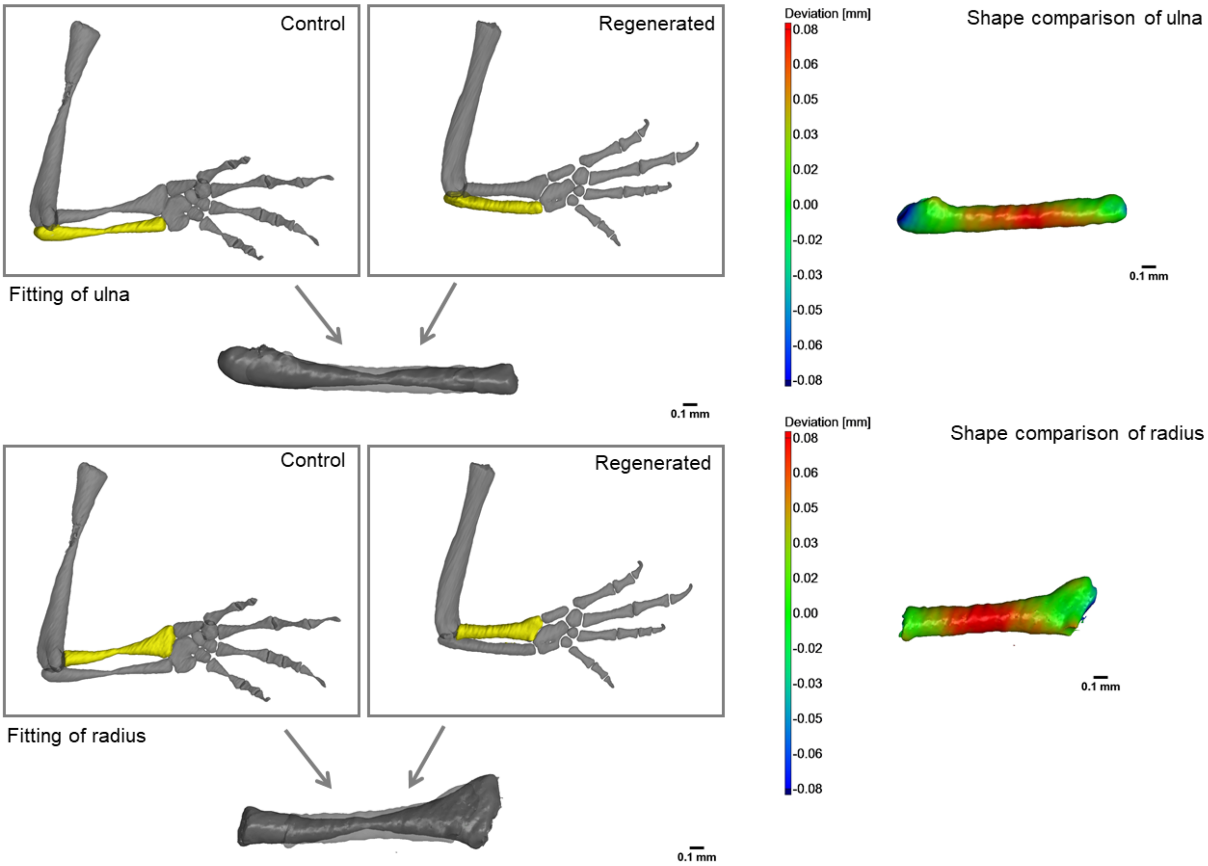

Figure 3.2: Shape comparison of ulna and radius of control and regenerated larval salamander limbs. There are no significant differences in the epiphysis. However, the diaphysis of control is narrowed compared to the regenerated limb.

3.2 3D-cell distribution in the regenerative muscle-skeletal system

During the measurements of salamander limbs with a conventional X-ray source at CEITEC BUT, we noticed very good contrast and resolution in tomographic data where the individual cells were detectable. However, automatic detection of the cells was not possible (Fig. 3.3). In synchrotron facilities, the small angular source size, the high intensity and the nearly-parallel geometry of the X-ray beam make it possible to obtain high spatial resolution. Furthermore, applying phase contrast could help the contrast of cells where only cell nuclei were stained. Thus, we applied for a synchrotron experiment at Elettra synchrotron (Trieste, Italy). Our goal was to perform tomographic measurements of salamander limbs to quantify cells inside cartilaginous elements of developing salamander (*Pleurodeles waltl*) limb [4]. Mapping the cells, their orientation and extracellular matrix distribution in 3D during salamander limb development could be taken as an input for computational modelling. This section describes individual steps to perform such quantitative analysis.

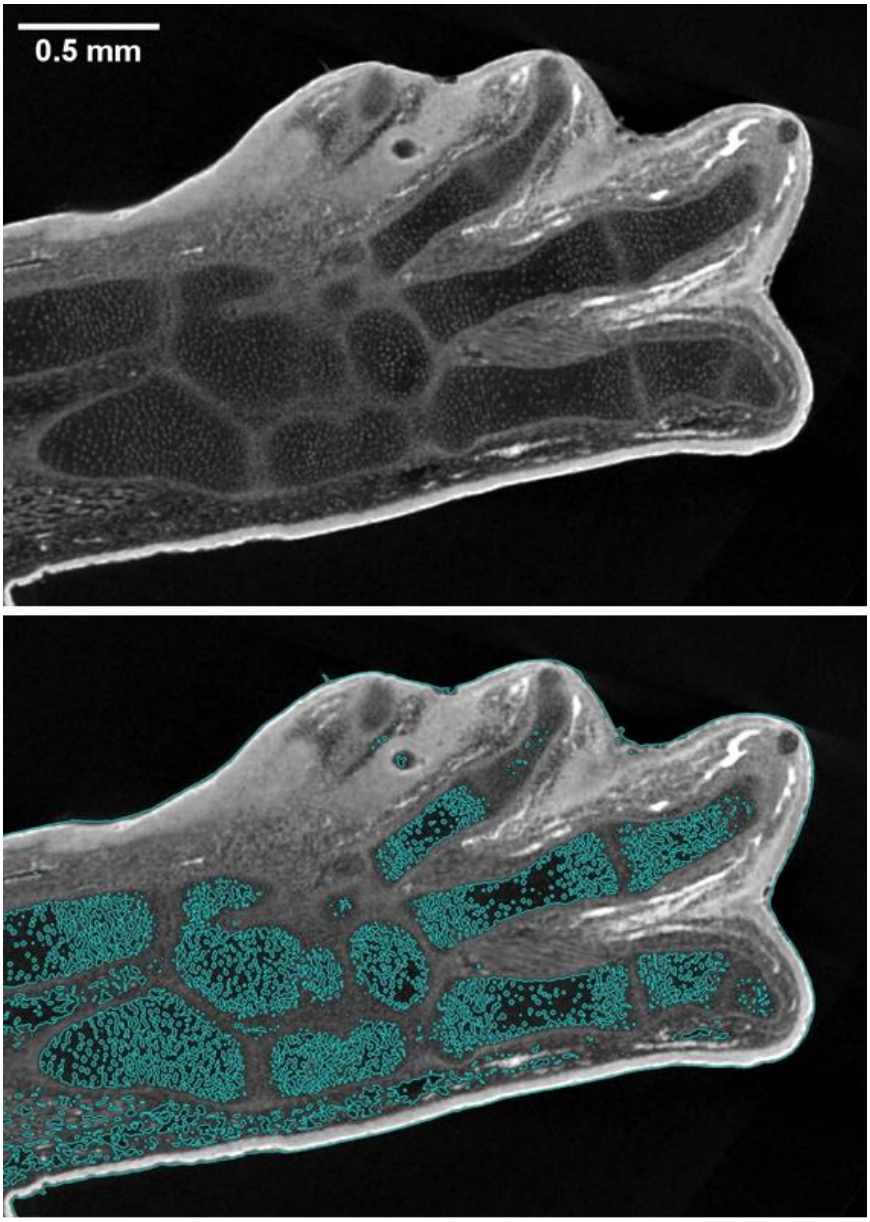

Figure 3.3: CT slice of salamander limb measured with conventional X-ray source. The upper image shows the original reconstructed data. White spots in cartilage represent cell nuclei. The blue line on the bottom image shows an attempt to segment the cells automatically. Errors are evident as connected regions of interest or missing some cells.

3.2.1 Number and density of cells within the extracellular matrix

The high spatial resolution (down to 1 µm) of synchrotron microCT at SYRMEP beamline at Elettra synchrotron achieved the cellular resolution needed for quantitative analysis of cell distribution. Also, thanks to phase-contrast, the borders of cells in cartilaginous elements have been distinguished.

To perform a quantitative analysis of cells, several steps were required. The complete procedure is described in detail in the published manuscript [4]: The first step was to segment individual cartilaginous elements (Fig. 3.4). However, the conventional segmentation algorithms failed on this task. Therefore, I used the freeware image analysis software ImageJ with its plug-in ABSnake. The provided steps included the determination of the starting contour for segmentation (done manually by the user), the gradient threshold to be used in edge detection and the number of iterations of the segmentation cycles.

Nevertheless, by applying a contour on the non-filtered tomographic slices, the iteration process did not converge to the cartilage border (Fig. 3.5 a–c) because of the irregular boundary of the cartilage. To avoid this problem, the contour was applied to the median-filtered images. After filtering, the iteration procedure converged, and the resulted contour was the smooth cartilage border. The final line copied the perimeter of the cartilaginous elements (Fig. 3.5 d–f). Then, the segmented data could be taken as input for further steps in the quantitative analysis [4].

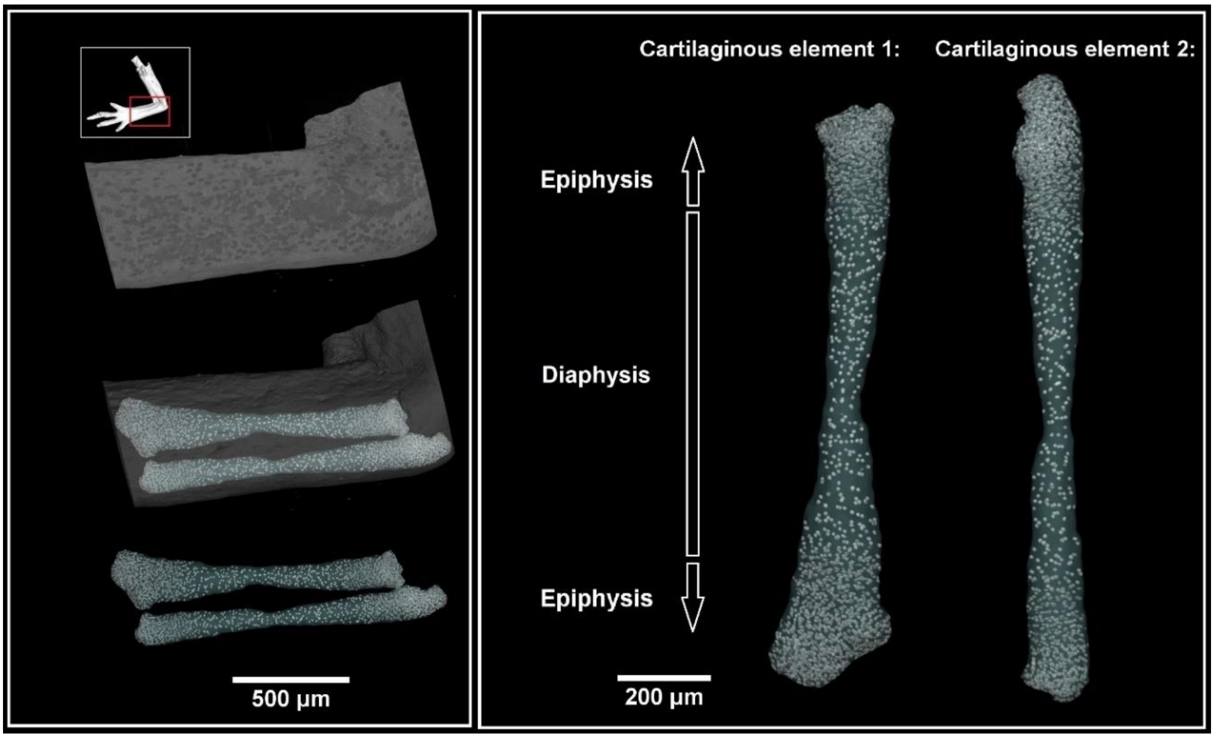

Figure 3.4: 3D visualisation of *ulna* and *radius* from an embryonic salamander limb (55A). White spots represent cell nuclei. Note difference density for epiphysis (high concentration of cells) and diaphysis (low concentration of cells). Modified from [4].

Another step was to count the cells, i.e. cell nuclei, inside segmented cartilaginous elements. The Pore3D software library [14] was used for this step. The 3D K-means clustering algorithm sorted data into three classes: the nuclei of cells, the extracellular matrix and the background. By evaluation of binarized data (comparison of Fig. 3.5 g and h), it is evident that some nuclei are connected into one blob (binary large object – blob). The red arrows show the example of connected blobs in Fig. 3.5.

Moreover, some border segments of the cartilage are miss-detected as cell nuclei (yellow arrows in Fig. 3.5). The erosion of the 3D data was the next step to getting rid of the miss-detected blobs. After the erosion, the data was well suited to determine the number of cells. Blob analysis [15] was performed to obtain the number of cells. The described procedure allowed us to determine the total number of cells, the volume of the cartilaginous elements, average size (given by the ratio of the volume of the whole element and number of cells) and density [4] (Table 3.1 and 3.2).

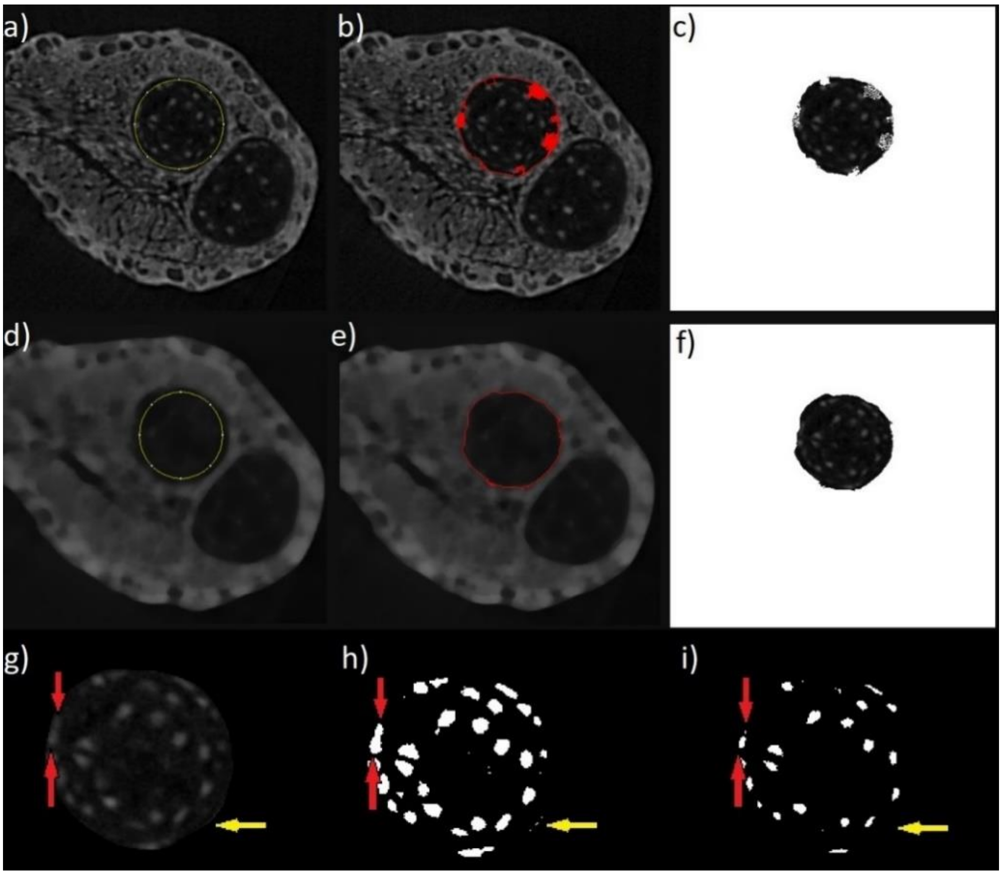

Figure 3.5: Individual steps of segmentation. (a–c) Shows the contour applied to non-filtered tomographic slices. (d–f) Shows the outline applied to filtered data. (g–i) Blob analysis in the Pore3D software. (g) Application of the 3D K-means clustering algorithm, (h) the results of the blob analysis, and (i) the eroded segmented image. Red arrows show two nuclei of the cells connected within the blob analysis. Yellow arrows indicate the light border of the cartilage [4].

Table 3.1: Quantified criteria in the *radius*.

	Epiphysis	**Diaphysis**	**Epiphysis**
Number of cells	888	429	595
Volume of the whole element [mm^3]	0.0052	0.0071	0.0027
Average size of one cell [mm^3]	5.81×10^{-6}	1.65×10^{-5}	4.47×10^{-6}
Density of cells [mm^{-3}]	171,926	60,791	233,684

Table 3.2: Quantified criteria in the *ulna*.

	Epiphysis	**Diaphysis**	**Epiphysis**
Number of cells	441	333	1040
Volume of the whole element [mm^3]	0.0023	0.0058	0.0050
Average size of one cell [mm^3]	5.28×10^{-6}	1.74×10^{-5}	4.85×10^{-6}
Density of cells [mm^{-3}]	189,309	57,401	206,360

Another way to describe the density of cells inside cartilaginous elements is to calculate the distance between cell nuclei. To perform this, the binarized dataset was taken as an input. To determine this parameter, the circumscribed spheres were created for each binary object, i.e. cell nucleus. Then, the distance between these spheres was described as the *gap* parameter in VG Studio software. By this definition, some values can be negative (overlap of the spheres). This type of analysis gives a similar result to Tables 3.1 and 3.2 and is shown by colour-coding in Fig. 3.6.

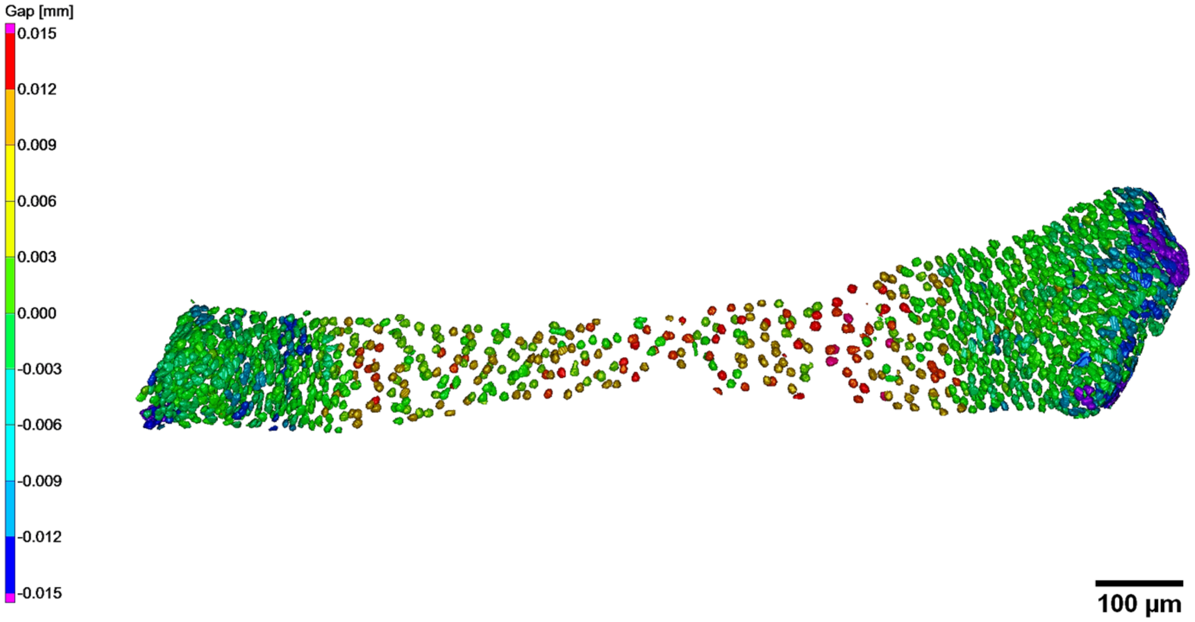

Figure 3.6: Calculating the distance between cell nuclei. The parameter *gap* indicates the minimum distance between the surfaces of the circumscribed spheres of two objects (i.e. cell nuclei).

3.2.2 The polarity of the cells in 3D

During analysing and segmenting cartilaginous elements, another interesting phenomenon was observed: When looking at the cells in the extracellular matrix, it seems that they are oriented, i.e. polarized, in specific directions. Moreover, the direction of polarization is different in different places in the cartilage. The tomographic slices with areas of polarized cells are shown in Fig. 3.7. To describe this phenomenon in detail and quantitatively, the 3D approach is needed again.

For this type of analysis, segmented binarized data were used. I used software VG Studio Max, with its module “Fiber orientation analysis”. Thus, every cell was considered the “fibre”, which means the direction of the axis of the element could be determined. Segmented data was registered in the coordinate system. The deviation angle of 0° corresponded to *yz* direction and blue colour. On the contrary, the deviation angle of 90° corresponded to *xy* direction and red colour. The result of the analysis is shown in Fig. 3.8.

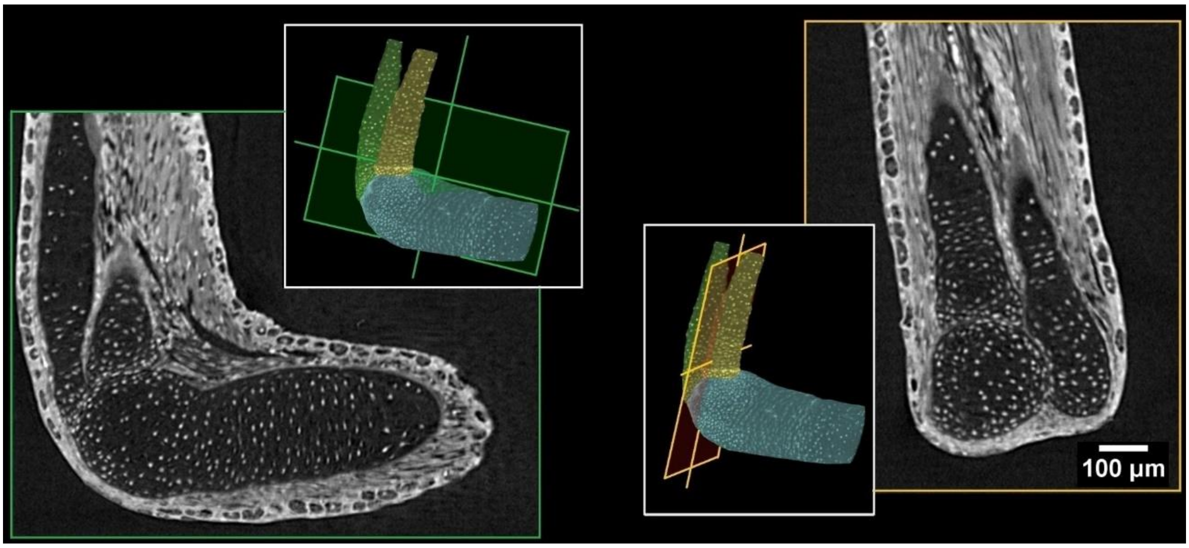

Figure 3.7: Tomographic slices in two orthogonal directions showing cellular resolution in tomographic slices [4].

"Fiber orientation analysis" provided detailed information about developing joint surfaces in the salamander limb. The impact of this observation is again described in the attached publication [4]: Orientation of chondrocytes in the developing joint correlated with the changing curvatures of joint surfaces. Also, the resolution and differential contrast was sufficient to map all chondrocytes' orientation inside the cartilage, which provided an essential foundation for future interpretation of the oriented cell behaviour during cartilage shaping. The results demonstrated that the predominant direction of chondrocytes in epiphyseal regions was different from rather central regions of the cartilage, where the cell density appeared low. In addition to this, superficial chondrocytes in epiphyseal regions were aligned with the developing surface of the cartilage (Fig. 3.8).

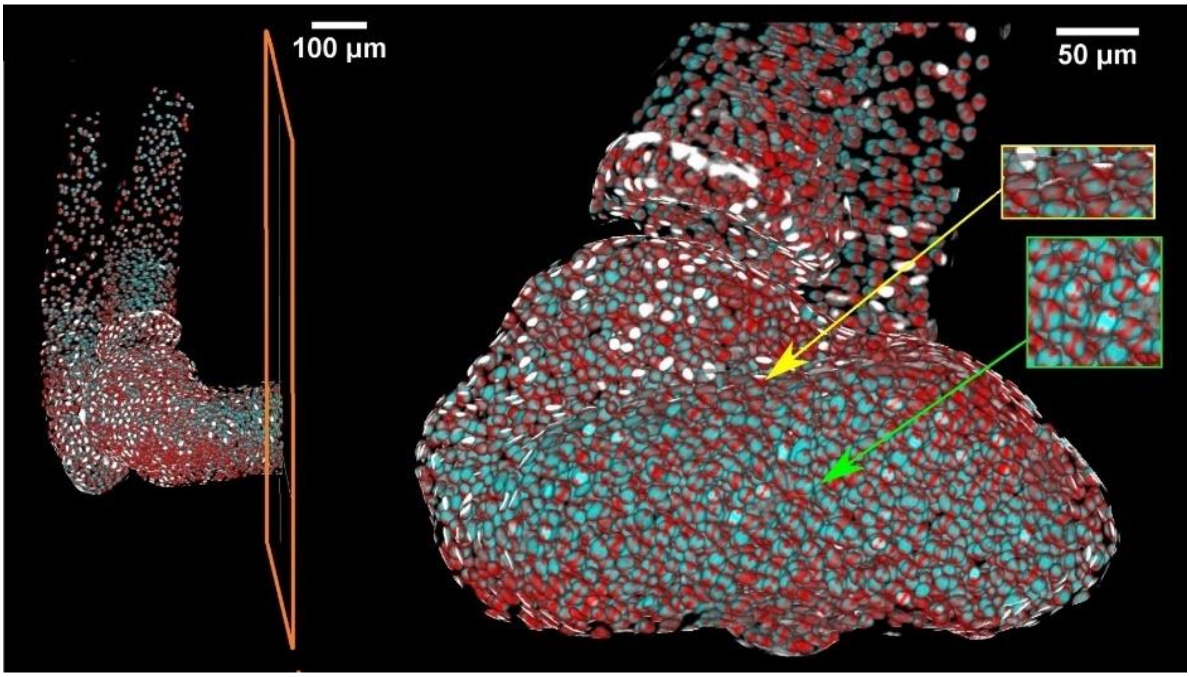

Figure 3.8: Detail of polarization of the cells on the salamander forelimb: Chondrocytes near-surface (yellow arrow) are aligned with the developing surface of the cartilage on the contrary with chondrocytes in the middle of the cartilage (green arrow). The orange plane on the 3D model indicates the position of the right image. Modified from [4].

3.2.3 Joint formation

Another area of interest was a joint formation within different stages of development. Here, we took advantage of the staining of the samples by PTA. In other words, we needed to be able to observe muscles and cartilage simultaneously. The development of muscles might guide cartilage and joint formation [16]. The visualization of these tissues in one 3D model showed some unexpected observations [4]: Three developmental stages were observed from a muscle-skeletal point of view. At the earliest analysed stage (41–42), only one small group of muscle around the elbow joint was found. However, different muscle groups (*biceps brachii*, *triceps brachii*, *brachioradialis* and *flexor carpi radialis*) were recognized in the following two stages.

Meanwhile, the elbow joint angle was decreased with the development of muscle. To calculate the elbow joint angle, the cylinders were fitted into humerus and radius and then, the angle between the cylinders' axes was measured. Interestingly, the decreasing elbow joint angle was observed with increasing developmental stages. The result of the analysis is shown in Fig. 3.9.

When looking at the visualisation of muscles in context with analysis of polarization of cells, there is a correlation between the cartilaginous cell polarity and attachment of the muscles. The chondrocytes next to the muscles' attachment points have a higher cell polarity. It means a correlation between the cell polarity inside cartilage and muscle attachment points. It is natural to speculate the mechanical force from muscle stretch may be delivered to attach point and then influence local chondrocytes' polarity. Hitherto unknown mechanisms can control chondrocytes' location and density together with cell polarity and muscle attachment points [4].

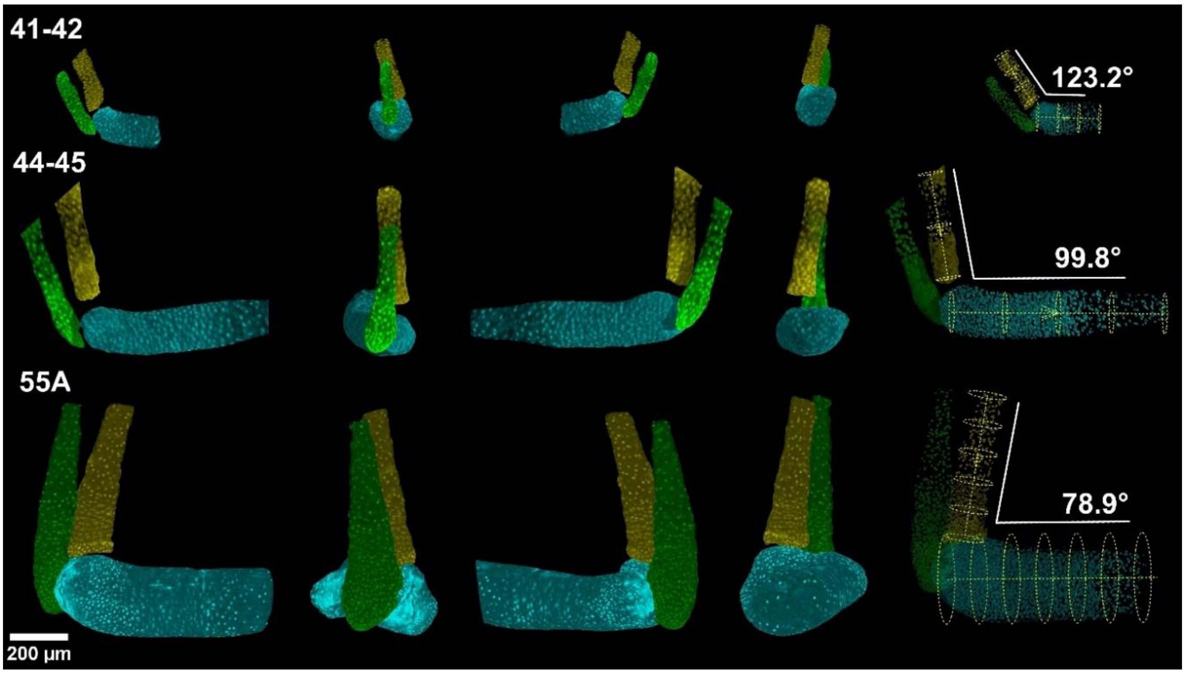

Figure 3.9: Development of the joint for three different developmental stages (41-42, 44-45 and 55A). The angle between *ulna* and *humerus* is decreasing with increasing developmental stage [4].

3.3 Adaptation of Proteus anguinus to dark habitats

When exploring regeneration salamander species, we mainly worked on typical modern organisms *Pleurodeles waltl* and *Ambystoma mexicanum*. However, looking to the other, not so common species could give a new insight into the regeneration capabilities of amphibians. Thanks to the strategic partnership with synchrotron Elettra and its location in Dinaric karst, we got an opportunity to meet another salamander species – *Proteus Anguinus*, also known as olm or simply proteus. Proteus is the largest cave tetrapod and the only European amphibian living exclusively in subterranean environments. However, specimens of proteus are rare and protected as proteus is currently classified as vulnerable [17].

For this reason, we accessed existing collections to avoid collecting them from nature. These animals died of natural causes, and their bodies were preserved (stored in 75% ethanol). We accessed the collection in Speleovivarium Trieste, Tular Cave Institute and the University of Ljubljana. We applied non-destructive staining and non-destructive imaging and then returned the specimens to the collection.

For this study, we wanted to cover more developmental stages of proteus, and thus we accessed different collections to visualise larval and adult stages. Specifically: larva, 3 weeks old, captive breeding originating from the Postojna-Planina Cave System, from the collection of the Tular Cave Laboratory (Slovenia); juvenile, deceased at the collection site in a spring near Metković (Croatia), from the collection of the Department of Biology, Biotechnical Faculty, University of Ljubljana (Slovenia); adult, collected in Postojna-Planina Cave System (Slovenia, 1989), died in captivity of the Speleovivarium in 1999, from the collection of the Speleovivarium Erwin Pichl (Italy) [18].

Figure 3.10 shows 3D reconstructions of soft tissues in the head of proteus for three developmental stages. We focused on cartilaginous chondrocranium, brain and sensory organs, as olfactory epithelium and the presence of eyes.

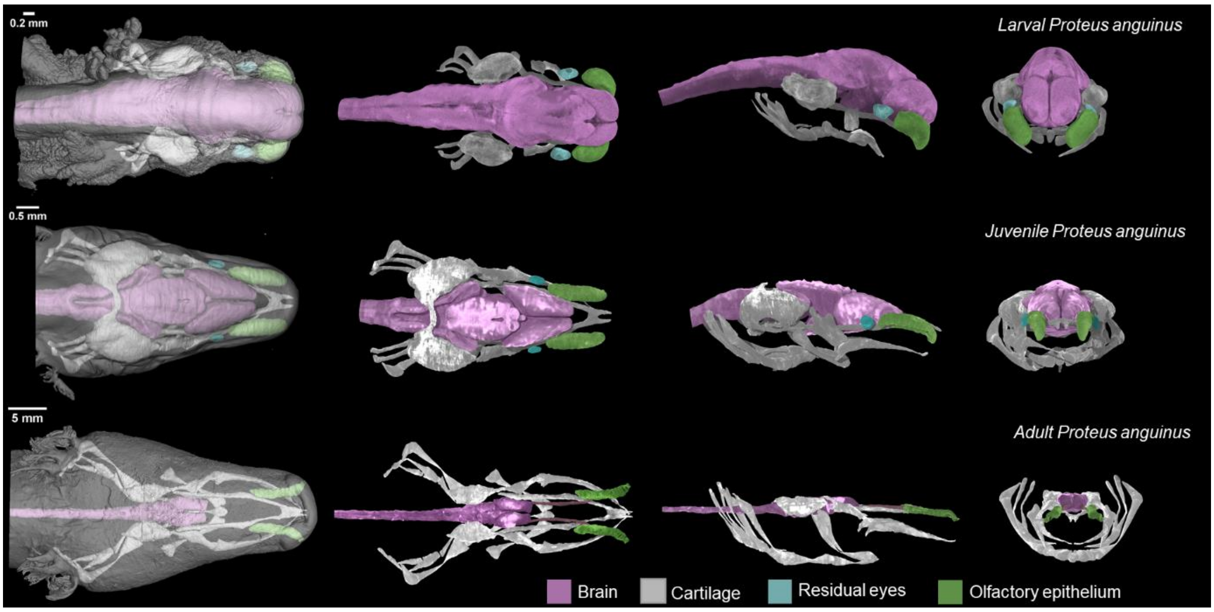

Figure 3.10: 3D reconstructions of proteus head. Larva (top), juvenile (middle) and adult (bottom]. Images in the first column show semi-transparent 3D renderings of the head with skin in dorsal view. Dorsal, lateral and frontal views of the segmented internal soft structures are shown in the second to the fourth column [18].

Also, we compared proteus with *Ambystoma mexicanum*, also known as the axolotl, to make a model comparison between cave- and surface-dwelling paedomorphic salamanders. The visualisations and detailed commentary can be found in the published manuscript [18]. By microCT scanning with a conventional source, we got excellent data quality, and single cells could be identified in cartilaginous elements. However, even though cells can be seen by the human eye, their automatic segmentation and quantification can be further challenging. Based on our partnership with Synchrotron Elettra and as this project was created in close cooperation with this institution, we decided to go also for synchrotron experiments. A comparison of the conventional and synchrotron X-ray microCT is reported in Fig. 3.11. Here, I show the potential of synchrotron imaging on larvae of *Ambystoma mexicanum* in the head structures (brain and eye). Such data can be used for mathematical modelling regarding joint shaping [19] or more general regenerative dynamics in various skeletal and non-skeletal tissues.

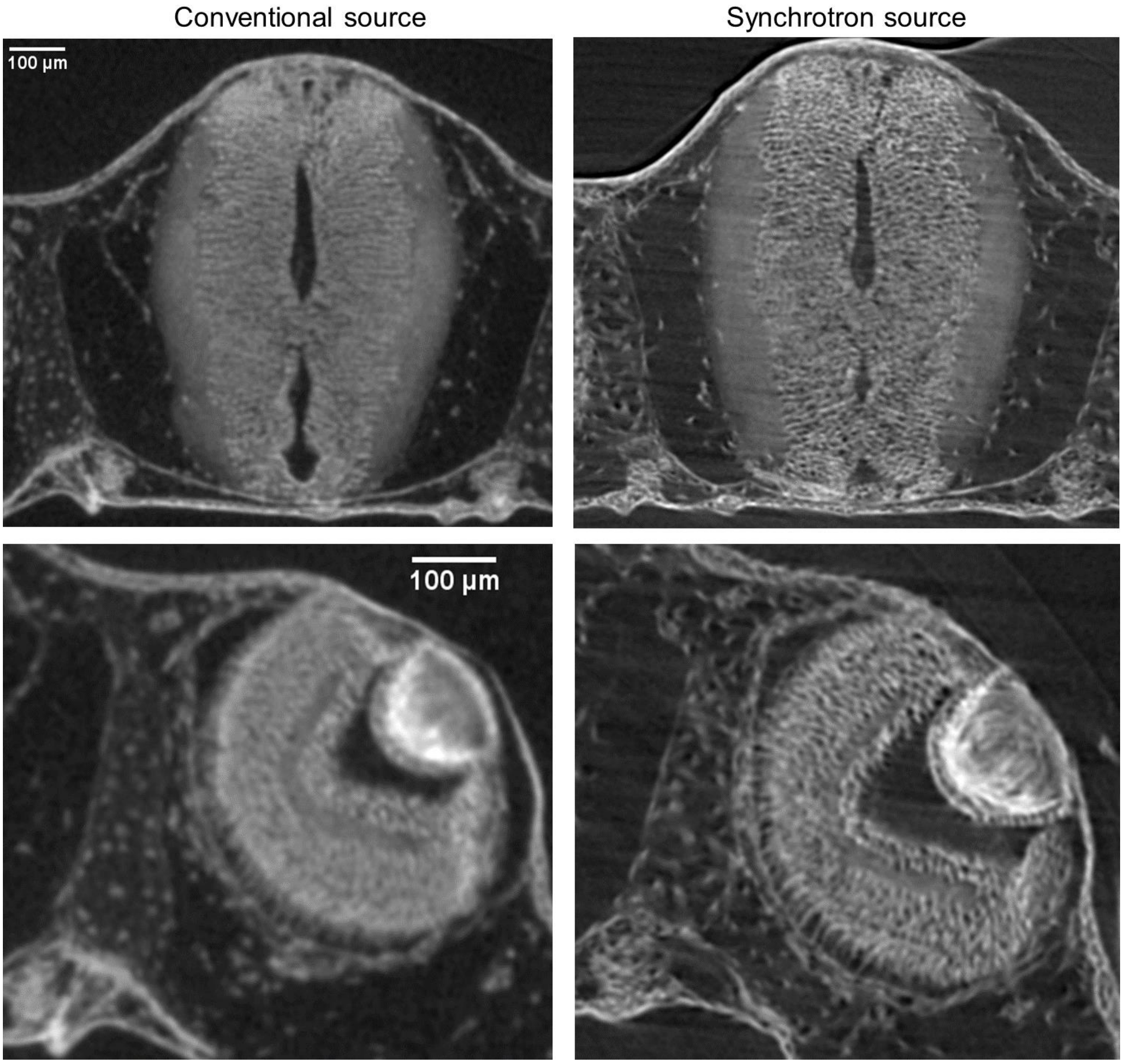

Figure 3.11: Comparison of conventional and synchrotron sources. The top images show the brain of *Ambystoma mexicanum* larvae, and the bottom images show its eye.

3.4 Vertebrate cartilage growth studied on mouse embryos

Cartilage is the core of embryo growth and shaping before the bone forms. It is an essential skeletal and supportive tissue in our body. The shape and size of each cartilage element result from complex developmental processes. Cartilage elements vary widely in shape: they may be simple shapes like rods or bars (Meckel, cartilage templates of the future long bones and ribs) or sheet-like structures (in the head) but can be highly complicated with many irregular shapes [20, 21].

The craniofacial region consists of diverse embryonic cell types, including skeletal, muscular and nervous components [22]. The final shape of the face strongly depends on the geometry of the skeletal elements and their interaction with adjacent soft tissues such as muscles and the nervous system [20, 21]. Numerous congenital craniofacial abnormalities affect the face's form and function, and explanations of these malformations still await the understanding [23]. According to the World Health Organization, genetic disorders have an incidence of 3 % in the human population [24], and they are causal for up to one-quarter of all reported neonatal deaths [25]. Thus, contextual visualisation of embryonic development is critical to clarify the origins of malformations [10].

The mouse model is a compelling experimental model: it is a mammalian system with similar embryology, anatomy and physiology to humans; genes, proteins and regulatory programs are largely conserved between humans and mice [26]. To understand the changes in dimensions of chondrocranium growth at major developmental stages, we created 3D reconstructions of cartilaginous chondrocranium (Fig. 3.12). Based on 3D microCT reconstructions of mouse chondrocranium, we were able to report a novel principle of vertebrate cartilage growth based on introducing transversally-oriented clones into pre-existing cartilage [20]. The microCT analysis, followed by 3D quantification, has enabled the understanding of complex morphological aspects of face development [20, 21, 27].

In this project, it was crucial to distinguish mesenchymal condensations, cartilage and bone. Mesenchymal condensations are the stage before early cartilages start to form, and thus, the segmentation in microCT data was challenging. On the opposite, the transition of cartilage to bone was clearly recorded in the data as synchondroses are involved in this transformation. Synchondroses have a lower density than cartilage and newly formed bone, and thus, they can be detected as darker areas with lower attenuation (Fig. 3.13). Since growth plates or synchondroses are oriented towards a specific direction, expanding cartilage in other dimensions was unclear and required further investigation [20].

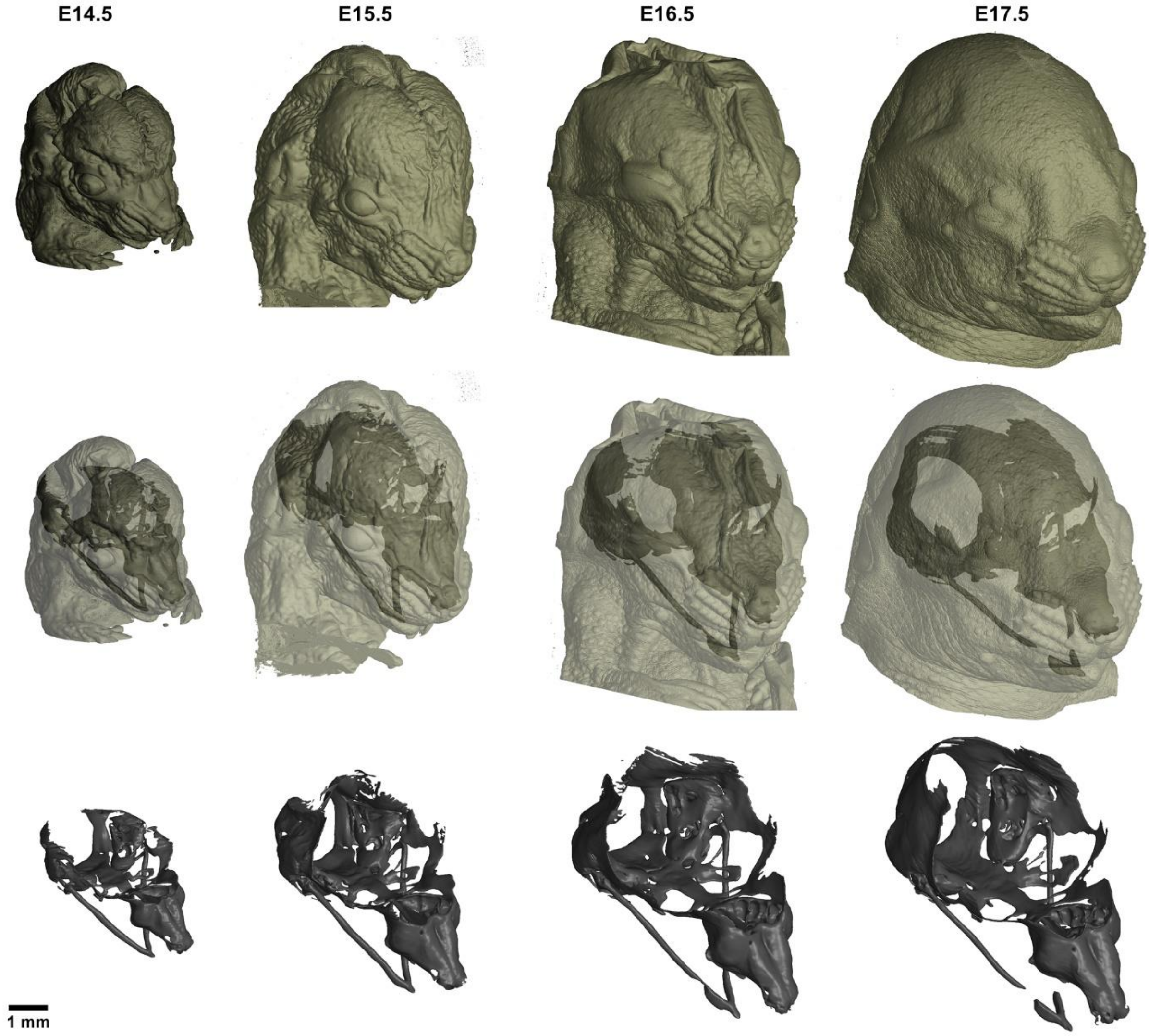

Figure 3.12: 3D reconstructions and segmentations of cartilaginous chondrocranium in mouse embryos, developmental stage E14.5-E17.5 The top row shows the 3D rendering of skin. The middle row shows semi-transparent heads with segmented chondrocranium. The bottom image shows only cartilaginous chondrocranium.

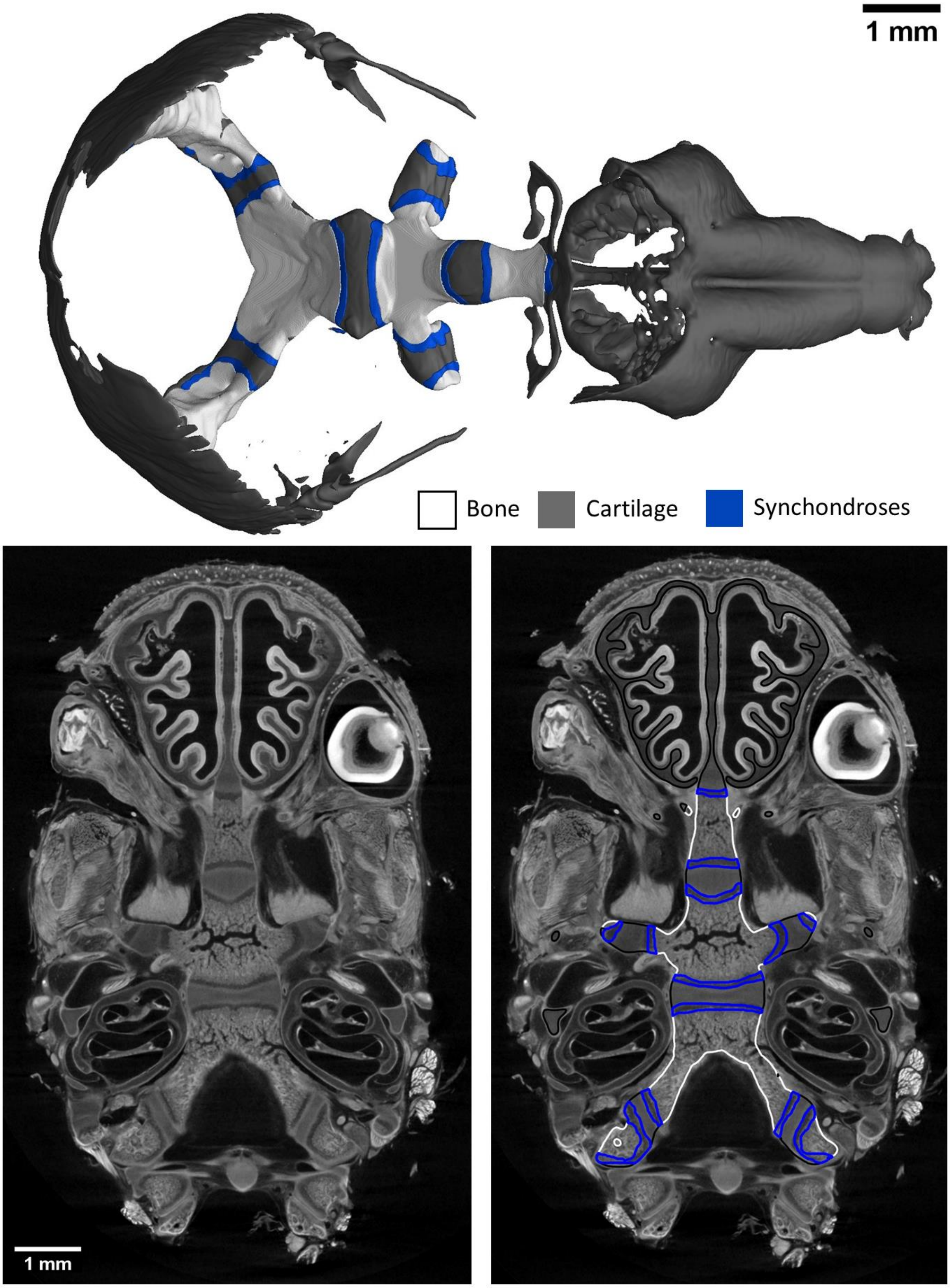

Figure 3.13: 3D reconstructions of cartilage, bone and synchondroses in mouse 2 days after born (P2). A corresponding CT slice with segmented structures is shown in the bottom part.

3.4.1 Wall thickness analysis

By observing the results of cartilaginous nasal capsules from different developmental stages, E14.5 generally establishes the shape of the structure. Nevertheless, from E14.5 until E17.5 the cartilaginous nasal capsule is accurately scaled up with significant geometrical tuning. Therefore, we wanted to understand the mechanism of scaling and whether cartilage thickens or narrows during development. We applied wall thickness analysis in software VG Studio MAX to study this process. The analysis inscribes the sphere to the STL model, and the diameter of the inscribed sphere is taken as the "wall thickness". Surprisingly, the thickness of the cartilaginous sheets did not change as much as the other dimensions during nasal capsule growth. Thus, the sheet-shaped cartilage expands mainly laterally (within the plane) during directional growth (Fig. 3.14) [20].

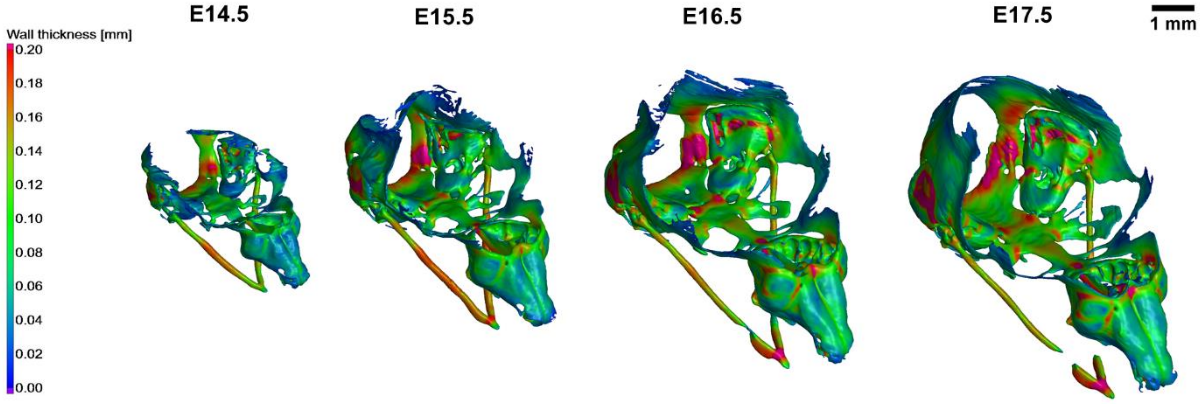

Figure 3.14: Wall thickness analysis of the cartilaginous chondrocranium of mouse embryos developmental stages E14.5-E17.5

3.4.2 Shape comparison

Also, we wanted to compare the shapes of the nasal capsules of major developmental stages and at five Wnt/PCP mutants (Wnt5a$^{-/-}$, Vangl2$^{-/-}$ and Ror2$^{-/-}$ together with Vangl2$^{+/-}$Ror2$^{+/-}$ heterozygous control). By simple look, the shape of the nasal capsules seemed very similar to one another for normally developing stages. However, we wanted some quantification to prove the exact shape of the segmented models. A typical way of comparison of 3D models is morphometric analysis. Traditional morphometrics relies on measurements such as linear distances, angles, weights or areas. However, most modern morphometric approaches are based on an analysis of landmarks. It means that set of landmarks is set on the 3D model. The assumption is that these landmarks are defined homologically across models. A particular landmark should unequivocally correspond to the same point across the stages etc. However, homology is a significant issue for morphometrics [28]. In our study, we defined the landmarks as shown in Fig. 3.15: Here, five representative distances were determined on the nasal capsule and these distances were measured for analysed developmental stages. Then, proportions were compared.

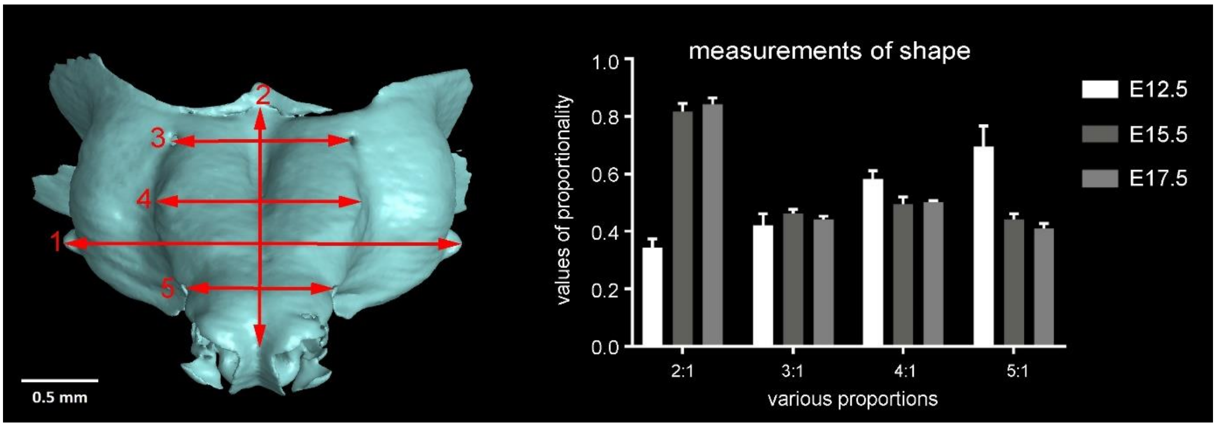

Figure 3.15: Morphometric analysis of E12.5, E15.5 and E17.5 stages. Red dimensions in the blue nasal capsule show the measurements used for morphometric analysis [20].

Even though morphometric analysis gave us logical and presumed data, we looked for further options on how to compare the shapes in a more intuitive demonstrative way that will not be dependent on the definition of landmarks. The best uniform option was given by the shape comparison analysis that is often used in the industrial sector for the comparison of two CAD/STL models. According to their septum, the nasal capsules were converted into STL files and registered in one coordinate system. Then, registered 3D models were compared (always the older one to the previous developmental stage) in a GOM Inspect Software by finding the closest distance between models with the searching angle of 30°. Finally, the same procedure compared E15.5 Wnt/PCP mutants to the same developmental stage of a wild-type control embryo. The result of the analysis is shown in Fig. 3.16.

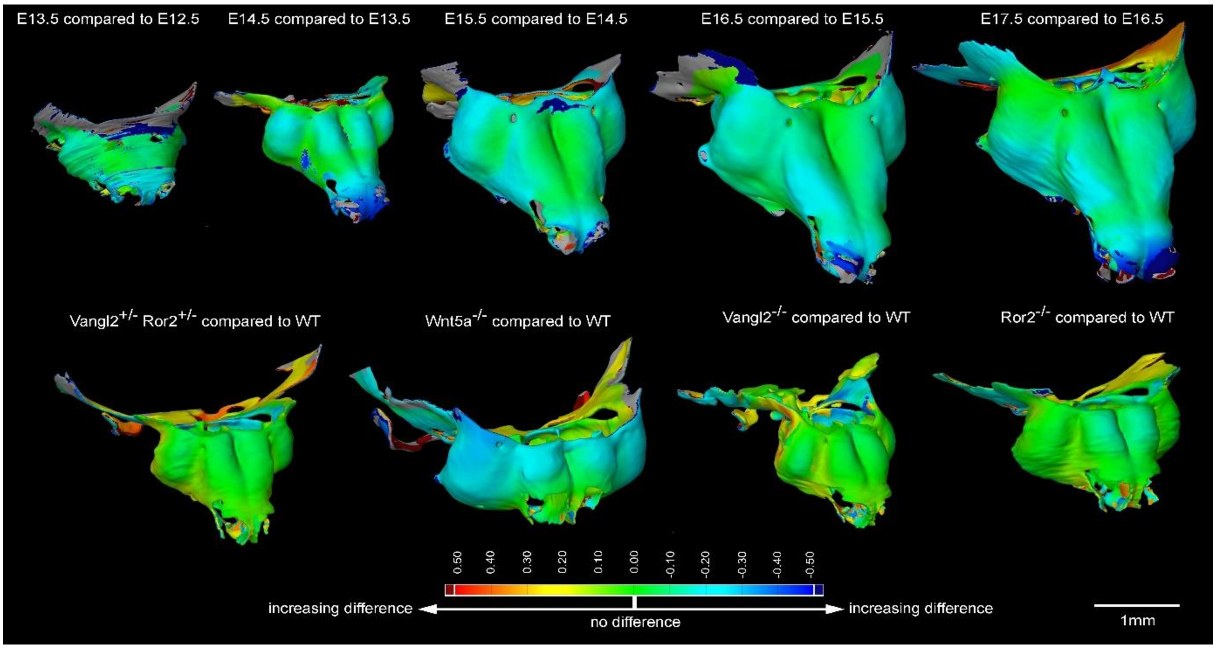

Figure 3.16: Shape comparison between control developmental stages and Wnt/PCP mutants. Colouration represents the incremental difference in the shape of the compared samples from green to red or blue colour [20].

3.4.3 Modelling of cell division based on microCT models

A significant advantage of segmented microCT 3D models is that they can be transformed into polygonal mesh suitable for other techniques such as 3D printing [8] or mathematical modelling. In this project, segmented cartilage was taken as an input to modelling uneven growth in shaping the nasal capsule. To exploit that, it was necessary to determine areas with different proliferation. To track and visualise the speed of proliferation, microCT data were combined with EdU labelling and fluorescence microscopy (Fig. 3.17). For each fluorescence image, a corresponding microCT slice was found and based on the number of tracked cells, sub-3D-models were created based on the original nasal capsule model. By tracking and matching the whole 3D microCT dataset with data from microCT, different proliferation was determined in 3D. More details on mathematical modelling can be found in the published manuscript [20].

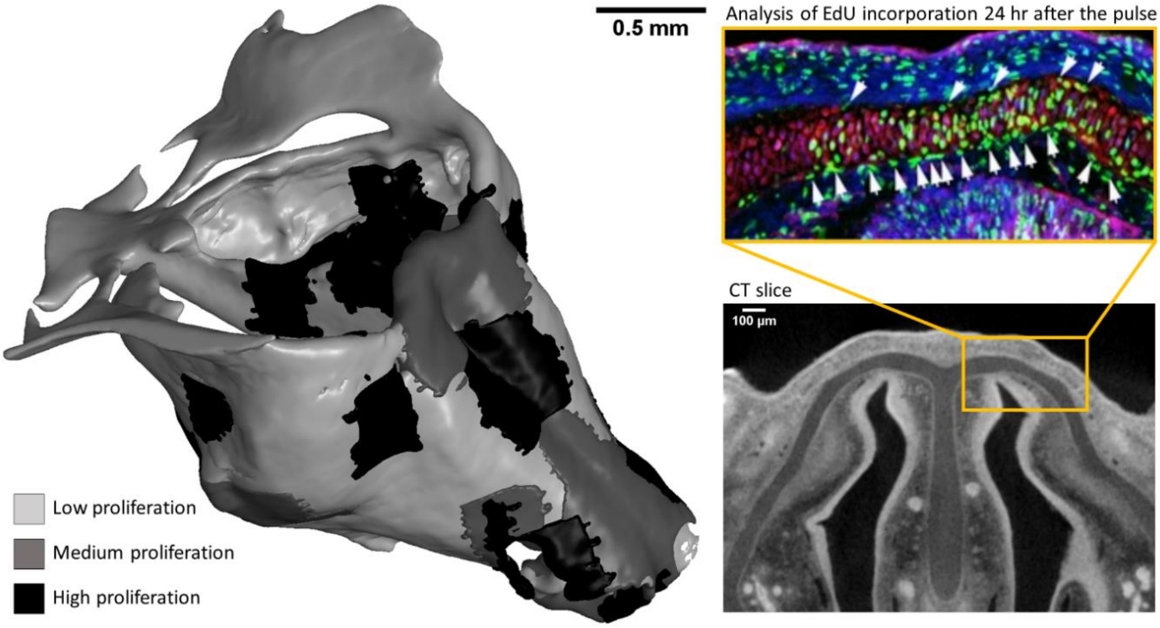

Figure 3.17: Input for modelling of uneven growth in a nasal capsule. The left image shows different cell proliferation in the 3D model. Right images show the creation of these growth zones based on matching EdU incorporation [20] with microCT slices.

3.5 Extraocular muscles development

It had been unknown how the individual extraocular muscles (EOMs) masses emerge from the individual muscle anlagen and how the development of their tendons and attachment points is coordinated. They are responsible for the coordinated movement of the eyeballs and vision. The basic EOM pattern is shared among all vertebrate classes. They include four recti muscles and two oblique muscles for eyeball movement [29-31]. Fig. 3.18 shows the anatomy of EOMs, and their responsible movements are described in Table 3.3.

This project investigated the morphogenesis of extraocular muscles (EOMs). While significant knowledge of the mechanisms of differentiation and patterning within individual tissues has been attained, much less about the patterning of different adjacent tissues [32, 33]. The study of muscles is usually done by confocal microscopy or optical projection tomography. However, these methods can visualize specific tissues such as muscles, but they do not give information about other anatomical structures such as eyeballs, cartilage, tendons etc. So knowing the position of the eyeball, lens and EOMs in the context of the whole head gives essential information about the developing structures.

This project aimed to build a precise spatiotemporal map of EOMs and quantify changes between developmental stages and genetically modified mice or after inhibitor treatments. By creating microCT 3D reconstructions, we identified a time window in which individual EOMs emerge from a unique muscle anlage and establish insertions in the sclera [34]. Also, connective tissue, tendons, and attachment points were visualized to determine whether they are derived from neural crest lineage.

The detail of this project can be found in the published manuscript [34]. This chapter then describes microCT analysis and quantitative measurements as ventralization of the eyeball or distance of *superior rectus* muscle from the eyeball.

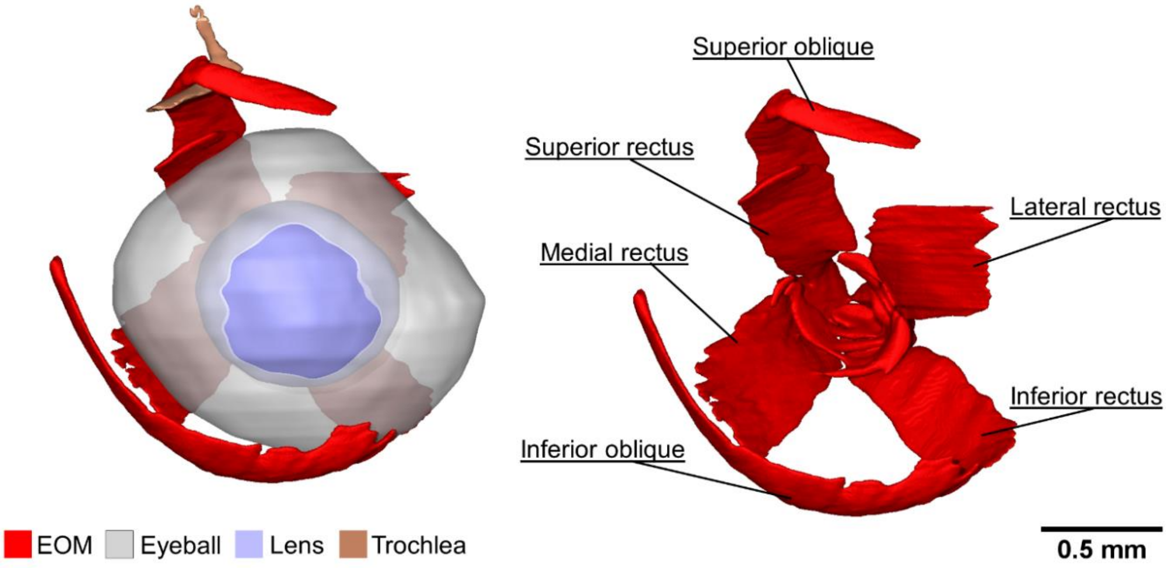

Figure 3.18: 3D reconstruction of extraocular muscles (EOM), eyeball, lens and trochlea in mouse embryo head 17.5 days post-fertilisation.

Table 3.3: Extraocular muscles and their responsible movement of the eye [35].

Name of the muscle	Responsible movement
Superior oblique	Downward and outward
Superior rectus	Upward
Lateral rectus	Outward
Medial rectus	Inward
Inferior rectus	Downward
Inferior oblique	Upward and outward

3.5.1 Ventralization of the eyeball

By PTA contrasting and subsequent segmentation of microCT data, we got a precise spatiotemporal atlas of the development of EOMs, eyeball, lens and optic nerve. We got information on these structures in one 3D dataset. Besides that, we observed these structures in the context of developing cartilage and the skin of the mouse embryos. To have the context of the developing structures was crucial when comparing normal development with genetically modified embryos. For BMS493-treated embryos, we noticed that eye of the mutant “looks down” compared to the control one. In other words, there is a ventralization of the eyeball. The ventralization for mouse embryos 13.5 days post fertilisation is shown in Fig. 3.19. We wanted to have a specific number representing the changes between the mutant and the control to describe this phenomenon. Therefore, we decided to measure the angle of inclination.

In geometry, the angle can be defined as the figure formed by two rays meeting at a common endpoint. For our purpose, we needed the definition of these two rays that will fit the geometry of the developing eye. Firstly, we fitted geometrical objects to selected biological structures: Two spheres were fitted to the eyeball and lens, and one cylinder was fitted into the eye nerve. Secondly, the first ray was defined as the axe of the cylinder and the second ray was defined as the vector for the nearest distance between eyeball and lens. Finally, the angle of inclination was den calculated as the angle of these two rays. The individual steps of this analysis and the computation result are shown in Fig. 3.20. In this way, the actual number was determined that describes the observed fact that mutant looks down in comparison with control.

Figure 3.19: Comparison of control and genetically modified (BMS493-treated) mouse embryos 13.5 days post-fertilisation. The top images show the 3D rendering of the skin of the whole head. The middle images show semi-transparent skin with the segmented eyeball, lens, optic nerve and EOMs. The bottom images show only segmented structures. The perspective of the eyeball in the whole head shows ventralization in the mutant.

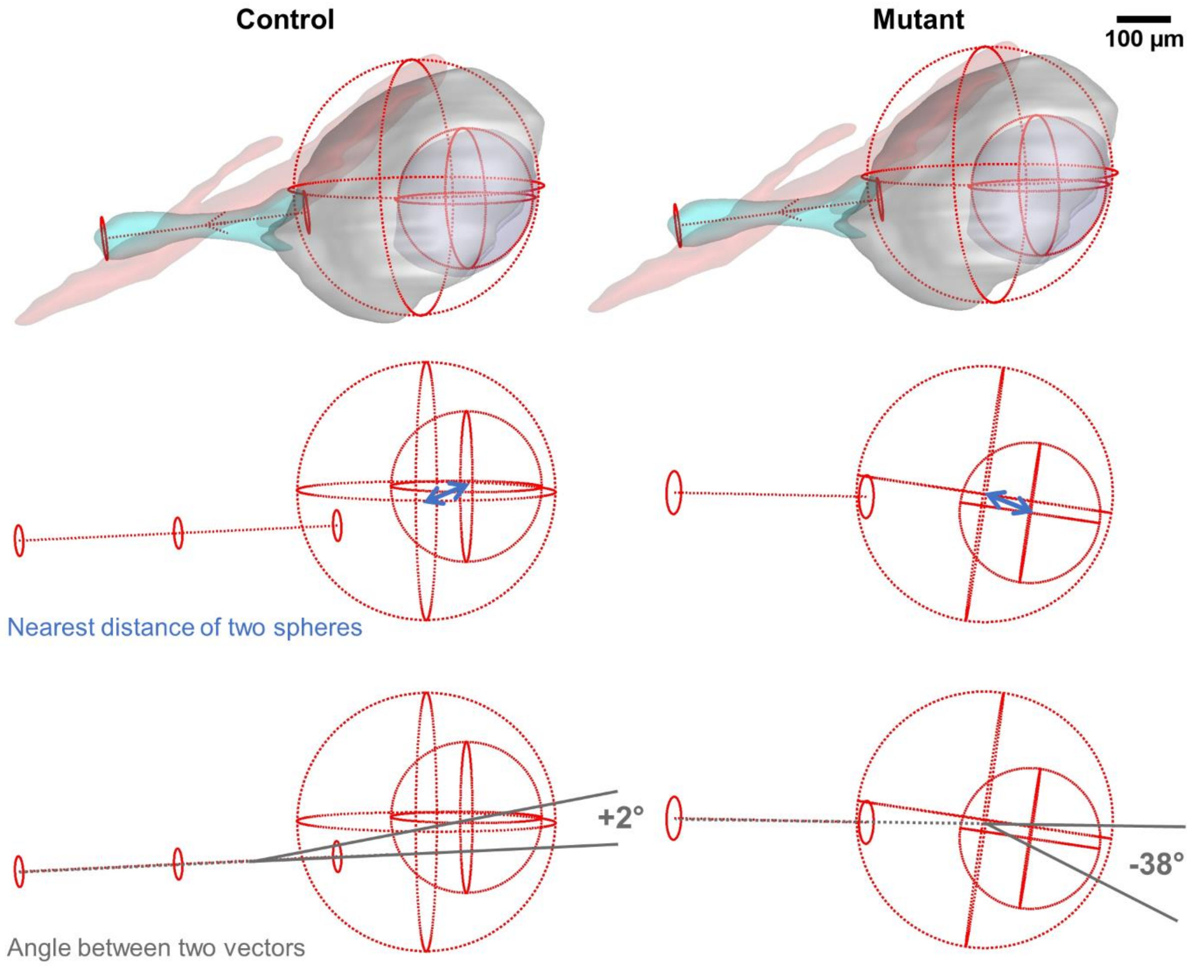

Figure 3.20: Fitting geometrical objects to biological structures. A cylinder is fitted to the optic nerve, and spheres are fitted to the eyeball and lens. The difference between a control and a mutant (BMS493-treated) is 40°.

Another interesting phenomenon observed in 3D models was the distance of the *superior rectus* muscle from the eyeball. It seemed that this muscle was going very near to the eyeball in the control embryo. However, at the mutant, the distance seemed farther. Firstly, we looked at tomographic slices of the reconstructed volume. As there is a ventralization of the mutant eyeball, it is very challenging to find corresponding orientation for two volumes of two different samples. Based on this fact, I fitted one point to the muscle and one point to the eyeball, but also this procedure is dependent on the operator, so I further looked for other options on how to determine this distance. The best option seemed to fit additional volume between the muscle and the eyeball. In the second step, I subtract the segmented structures from the volume. In the third step, I looked at the "thickness" of the gap between the structures. The result of this analysis is shown in Fig. 3.21. By calculating the thickness of this gap, the procedure becomes fully automatic and is not dependent on the operator. The manually measured distances can serve as the control for the automatic wall thickness analysis.

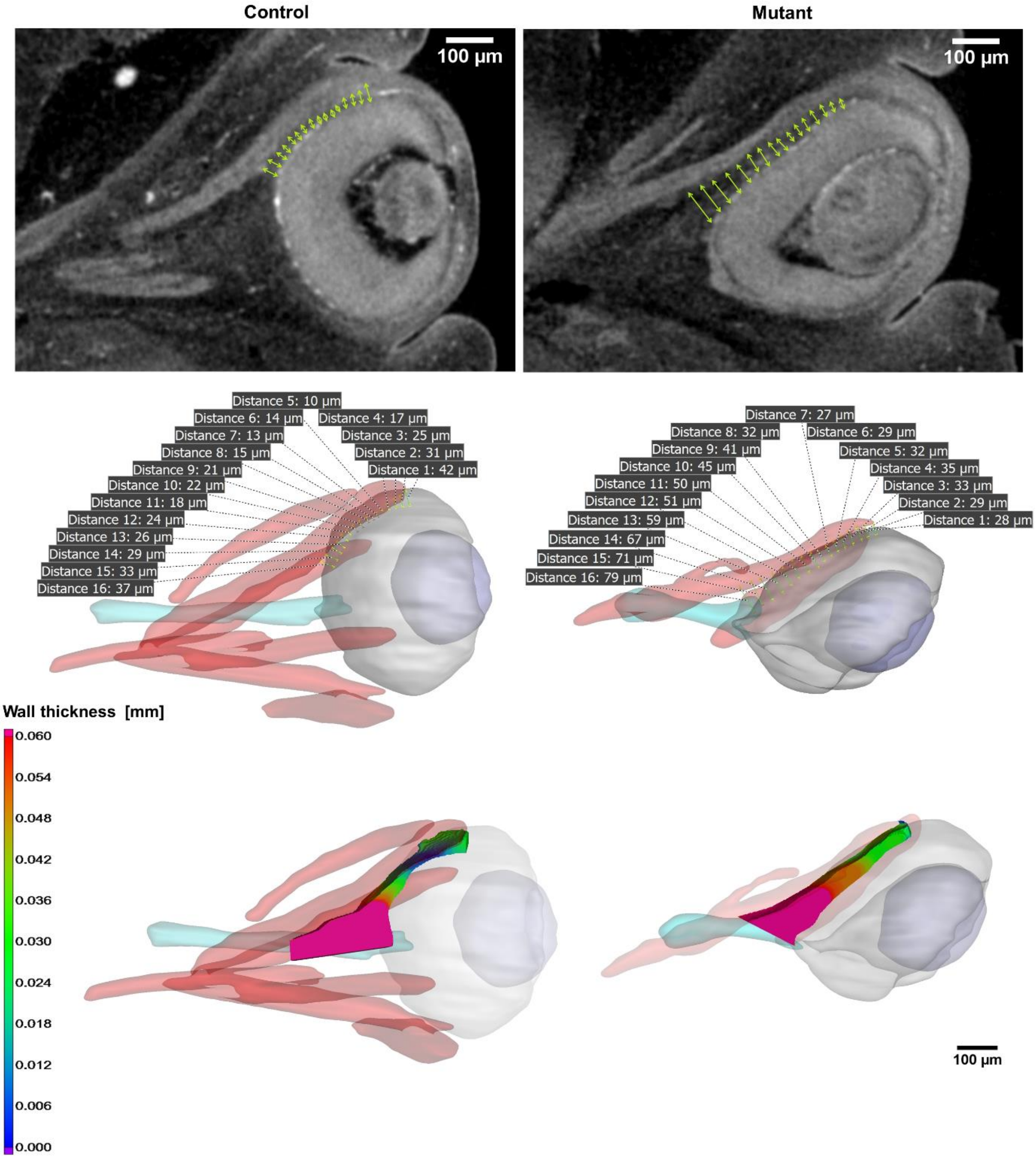

Figure 3.21: Measurement of distance between *superior rectus* muscle and eyeball for control and mutant embryo (BMS493-treated) 13.5 days post-fertilisation. The top images show CT slices, and green arrows indicate the distance to be measured between the muscle and eyeball. Middle images show manually measured distance. The bottom images show distance measured in 3D by determining wall thickness on volume inserted between the muscle and the eyeball.

4 Combination of microCT with other methods

4.1 Neck muscles and associated connective tissues

Neck muscles have remained poorly defined due to their complex morphogenesis and dual mesodermal origins [36]. The neck is composed of approximately 80 skeletal muscles that allow head mobility, respiration, swallowing, and vocalization processes in humans. A robust network of muscles ensures these processes at the head-trunk interface, a transition zone subjected to a spectrum of human muscle diseases [37-39]. Describing the embryology of the distinct muscle groups is crucial to understanding the mechanisms underlying specific muscles' susceptibility to muscular dystrophies. While myogenesis at the cranial and trunk levels has been studied extensively, the developmental mechanisms at the basis of neck muscle formation are poorly documented and often debated [40].

To describe the origins of different muscle groups, we combined immunostaining on sections and 3D microCT reconstructions of the neck and pectoral girdle of control and two genetically-modified embryos (Tbx1-/- and Pax3-/-) [36]. All samples were 18.5 days post-fertilisation. Because of the larger size of this developmental stage and possible limited staining penetration, we decided to cut off the area of interest for scanning. The cutting helped penetration a contrasting agent (PTA) into the sample. In other words, there was a dissection of the cervical region (including the mandible and scapular components). Thus, the staining time was reduced to 10 days. Another step for creating a 3D map of a neck region was to define the muscles of interest for 3D segmentation. When applying the staining procedure to soft tissues, segmentation is based on grayscale value and anatomical shape. However, using these criteria on muscles is quite challenging as they are hard to distinguish. To validate the neck muscles, we combined microCT data with immunostaining. Immunostaining clearly showed the individual muscles, but only on eight sections (Fig. 4.1) in the sample. In opposite, the resolution of microCT scanning was 5.7 µm for all samples but with lower differential contrast. The data showing both immunostaining and CT slices are shown in Fig. 4.2. When we combined information from both techniques by tracking marked muscles from immunostaining throughout microCT volume, we were able to get high-resolution reconstructions for muscles and skeletal elements in the context of the whole mouse embryo (Fig. 4.3).

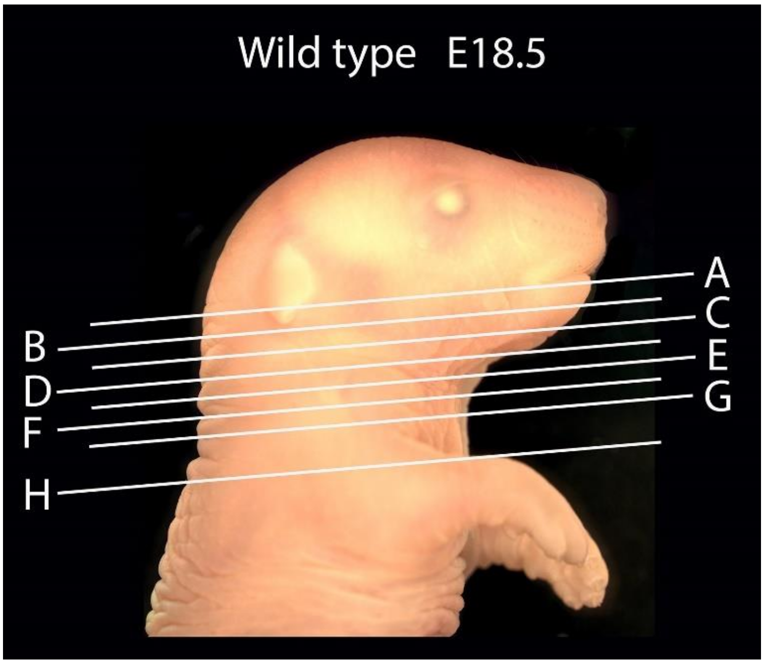

Figure 4.1. Mouse embryo 18.5 days post-fertilisation. Eight sections (A-H) indicate the planes of immunostaining that were subsequently matched with microCT data [41].

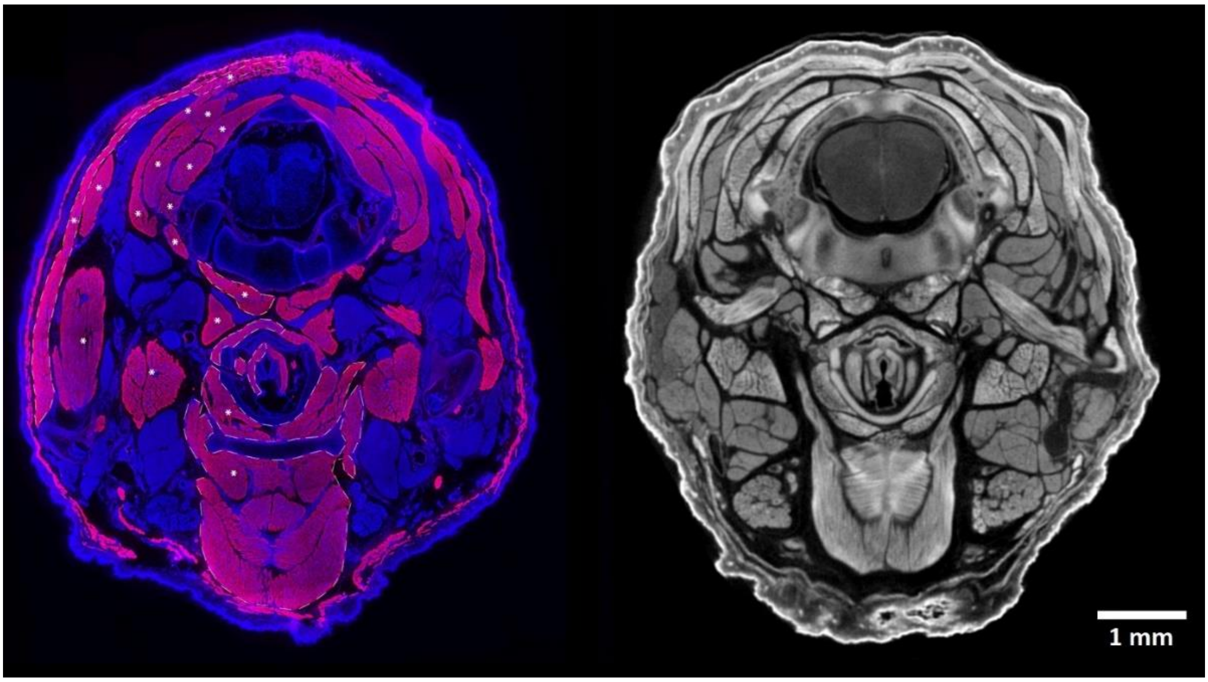

Figure 4.2. The immunostaining section (left) and corresponding CT slice of a mouse embryo (18.5 days post-fertilisation). The pink colour shows the muscles, and white asterisks mark the muscles that need to be visualized in 3D. Note similar contrast for muscles and other tissues at microCT slice [41].

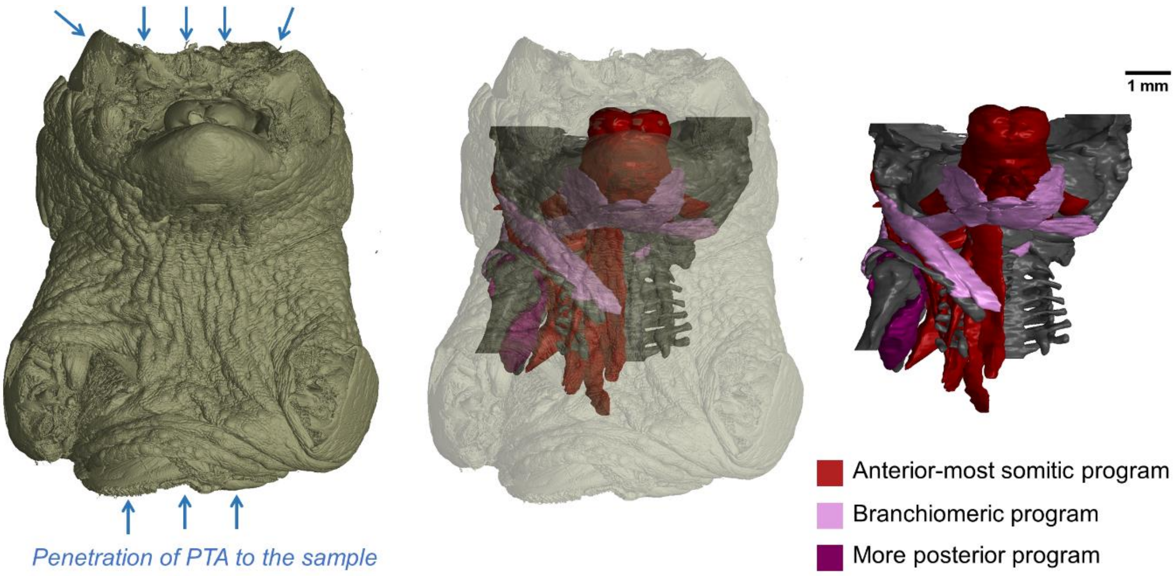

Figure 4.3: 3D reconstruction of the neck area of mouse embryo (18.5 days post-fertilisation). 3D rendering of skin (left), semi-transparent skin (middle) and segmented structures (right). Note cut in the area of head and abdomen. Blue arrows then indicate penetration of contrasting agent (PTA) to the sample in these areas.

Together with a 3D atlas of a control embryo, 18.5 days post-fertilisation, we analysed the effect of inactivation of Tbx1 and Pax3 genes on neck muscle formation, compared to the muscle phenotypes observed at cranial and trunk levels. Fig. 4.4 shows the reconstruction of the muscles and different colour-coding for anterior-most somatic, branchiometric and more posterior programs. Note the malformation of trapezius muscle affected in Pax3$^{Cre/Cre}$ and missing entirely in Tbx1$^{-/-}$. On the contrary, scapular muscles of the more posterior program are not significantly affected in Tbx1$^{-/-}$but missing in Pax3$^{Cre/Cre}$. Also, intrinsic laryngeal muscles were affected together with skeletal elements of the larynx. More details of biological observations can be found in the attached publications [36].

When comparing differences between genetically modified samples and developmental programs, we generated many 2D images with different transparency from the 3D models, different zooming etc. As a result, it became hard to get oriented in a generated data. For this reason, we began to look for the other way to put the 3D models into the publication so that anyone can access them without the need for specialised software. The best suitable option turned out to convert 3D models into interactive 3D PDF format. In this way, microCT data can be interpreted in small file format, readable on all operating systems using the widely used Portable Document Format (PDF). To convert the biological models into this type of document, I faced some challenges such as the size of the data, the colouring of the models with the conservation of sub-models hierarchy etc. First, I wrote down all the challenges that I faced during the creation of the model. Then, I formed a manual describing individual steps, starting with segmentation of the data and surface extraction to embedding models into interactive 3D PDF files. This manual was also published with an example of craniofacial structures, so anyone working with a 3D imaging technique can use our user-friendly protocol [10]. We believe that intuitive and interactive 3D PDF files have a great potential for data sharing, communication, and publications.

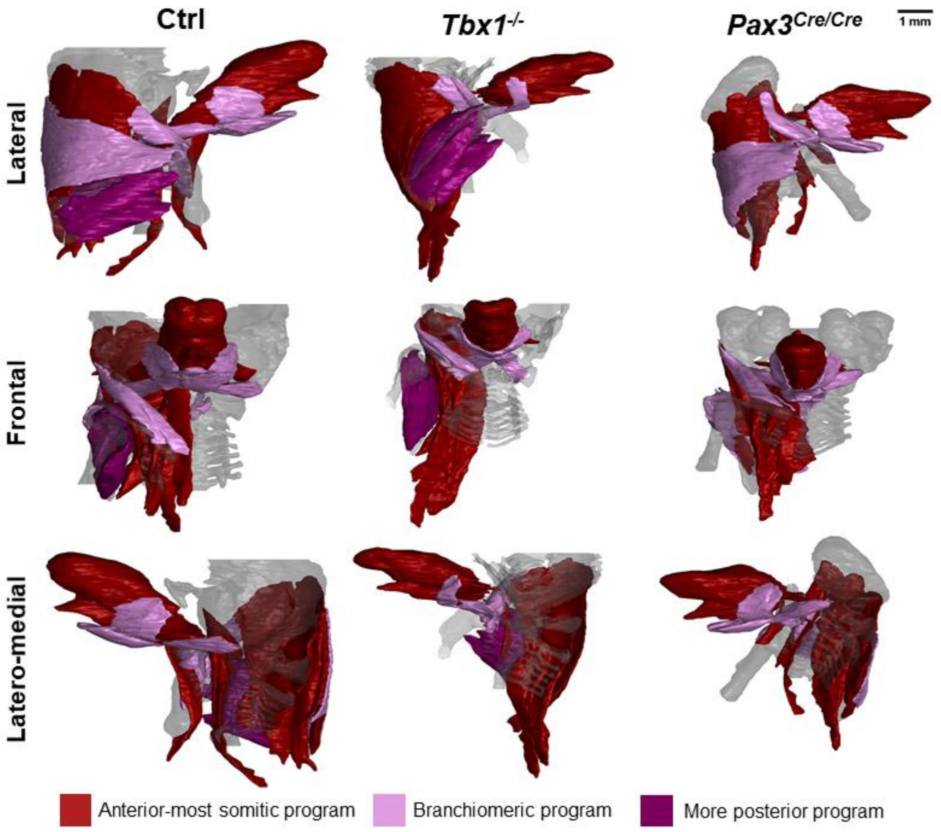

Fig. 4.4: 3D reconstructions of neck muscles in three mouse embryos: Ctrl (control) and two mutants (Tbx1-/- and Pax3Cre/Cre). Different colours correspond to different developmental programs.

5 Conclusion

The dissertation thesis reflects the current need for the biological community for precise 3D characterisation of studied structures. The microCT technique has shown great potential in developmental biology in recent years. However, there has been a lack of methodology for the quantitative characterization of 3D structures.

The particular applicability of this work is demonstrated in the research projects that have been published in impact factor journals. Specifically, my dissertation focused on studying salamander limbs' regeneration down to cellular level in different salamander species: Pleurodeles waltl, Ambystoma mexicanum and rare cave amphibian *Proteus anguinus*. Above that, a digital atlas of proteus was created involving different developmental stages and comparison with surface-dwelling axolotl. Since these 3D models are published online, scientists worldwide can access and use these models in their research, which is particularly valuable given the proteus is an endangered and protected animal.

Another animal in which structures were thoroughly analysed was mouse and mouse embryos, respectively. Also here, we accessed a diverse range of developmental stages together with genetically-modified animals. Particular attention was given to soft tissues in the head that have not been analysed by microCT before. We focused on cartilaginous chondrocranium and quantitative comparison of thickness and shapes. Similarly, muscles with attachment points, tendons, and supportive tissues were visualised and analysed, focusing on their different developmental programs. Many samples were scanned and segmented, so also here, we created a digital atlas containing microCT data of major developmental stages and relevant segmentations. This mouse embryo atlas was again published online so that anyone can access this valuable data. Thus, the effort and resources given to the 3D reconstructions can serve as the initial input for other scientific projects.

During the creation of 3D models and analysis, I faced many challenges: I fought with the contrast of soft tissues and staining protocols, unsolicited motion during microCT measurement and challenging data segmentation and 3D characterisation. In this work, I tried to address all topics relevant to microCT characterisation of biological structures in 3D, so any student or scientist dealing with a similar topic can take this document as a user-friendly recipe for their experiment.

6 References

[1] T. Zikmund, *M. Novotná, M.* Kavková, M. Tesařová, M. Kaucká, B. Szarowská, I. Adameyko, E. Hrubá, M. Buchtová, E. Dražanová, Z. Starčuk and J. Kaiser, *High-contrast differentiation resolution 3D imaging of rodent brain by X-ray computed microtomography*, *Journal of Instrumentation* **vol. 13,** (2018).

[2] *B. Metscher, MicroCT for comparative* morphology*: simple staining methods allow high-contrast 3D imaging of diverse non-mineralized animal tissues*, *BMC Physiology* **vol. 9,** (2009).

[3] B. Metscher, *MicroCT for developmental biology:* A versatile tool for high-contrast 3D imaging at *histological resolutions*, *Developmental Dynamics* **vol. 238,** (2009).

[4] M. Tesařová, L. Mancini, A*. Simon, I. Adameyko, M. Kaucká,* A. *Elewa, G.* Lanzafame**,** Y. Zhang, D. Kalasová, B. Szarowská, T. Zikmund, M. Novotná and J. Kaiser, *A quantitative analysis of 3D-cell distribution in regenerating muscle-skeletal system with synchrotron X-ray computed microtomography*, *Scientific Reports* **vol. 8,** (2018).

[5] M. Krenkel, A. Markus, M. Bartels, C. Dullin, F. Alves and *T. Salditt, Phase-contrast zoom tomography reveals precise* locations of macrophages in mouse lungs, *Scientific Reports* **vol. 5,** (2015).

[6] *C. Dullin, R. Ufartes, E.* Larsson, S. Martin, M. Lazzarini, G. Tromba, J. Missbach-Guentner, D. Pinkert-Leetsch, D. Katschinski, F. Alves and R. Roeder, *µCT of ex-vivo stained mouse hearts and embryos enables a precise match between 3D virtual histology, classical histology and immunochemistry*, *PLOS ONE* **vol. 12,** (2017).

[7] D. Pham, *C. Xu and J. Prince, Current Methods in* Medical Image Segmentation, Annual Review of Biomedical Engineering **vol. 2,** (2000).

[8] M. Tesařová, T. Zikmund, M. Kaucká, I. Adameyko, J. Jaroš, D. Paloušek, D. Škaroupka and J. Kaiser, Use of micro computed-tomography and 3D printing *for reverse engineering* of *mouse embryo nasal* capsule**,** Journal of Instrumentation **vol. 11,** (2016).

[9] P. Withers, C. Bouman, S. *Carmignato, V. Cnudde*, D. Grimaldi, C. Hagen, E. Maire, M. Manley, A. Du Plesis and S. Stock, *X-ray computed tomography*, *Nat Rev Methods Primers* **vol. 1,** (2021).

[10] M. Tesařová, E. Heude, G*. Comai, T. Zikmund, M. Kaucká,* I. Adameyko, S. Tajbakhsh and J. Kaiser, *An interactive and intuitive visualisation method for X-ray computed tomography data of biological samples in 3D Portable Document Format*, *Scientific Reports* **vol. 9,** (2019).

[11] E. Tanaka, Regeneration, Cell **vol. 113**, (2003).

[12] A. Joven, *A. Elewa and A. Simon, Model systems for* regeneration: salamanders, Development **vol. 146**, (2019).

[13] R. Diogo, *E.* Nacu *and E*. Tanaka, Is Salamander Limb *Regeneration Really Perfect? Anatomical and Morphogenetic Analysis of Forelimb Muscle Regeneration in GFP-Transgenic Axolotls as a Basis for Regenerative, Developmental, and Evolutionary Studies*, *The Anatomical Record* **vol. 297,** (2014).

[14] F. Brun, *L. Mancini, P. Kasae, S.* Favretto, D. Dreossi and G. Tromba, *Pore3D: A software library for quantitative analysis of porous media*, *Nuclear Instruments and Methods in Physics Research Section A: Accelerators, Spectrometers, Detectors and Associated Equipment* **vol. 615,** (2010).

[15] D. Zandomeneghi, *M. Voltolini, L.* Mancini, F. Brun, D. Dreossi and M. Polacci, Quantitative analysis *of X-ray microtomography images of geomaterials: Application to volcanic rocks*, *Geosphere* **vol. 6,** (2010).

[16] *L. Brunt, J*. Norton, J. Bright, E. Rayfield and C. Hammond, *Finite element modelling predicts changes in joint shape and cell behaviour due to loss of muscle strain in jaw development*, *Journal of Biomechanics* **vol. 48,** (2015).

[17] S. Stuart, J. Chanson, N. Cox, B. Young, A. Rodrigues, D. Fischman and *R. Waller, Status and Trends of Amphibian Declines and Extinctions Worldwide, Science* ***vol. 306,*** *(*2004).

[18] M. Tesařová, L. Mancini, E. Mauri, G. Aljančič, M. *Năpăruş-Aljančič, R. Kostanjšek, L. Bizjak Mali, T. Zikmund, M.* Kaucká, *F. Papi*, **J.** Goyens, A. Bouchnita, A. Hellander, I. Adameyko and J. Kaiser, *Living in darkness: Exploring adaptation of Proteus anguinus in 3 dimensions by X-ray imaging*, *GigaScience* **vol. 11,** (2022).

[19] E. Comellas, T. Duerr, J. Farkas, J. Monaghan and S. Shefelbine, *Integrating macromolecular data in a tissue-level computational model of vertebrate joint morphogenesis, 14th WCCM & ECCOMAS Congress* (2020).

[20] M. Kaucka, T. Zikmund, M. Tesarova, D. Gyllborg, A. Hellander, J. Jaros, J. Kaiser, J. Petersen, B. Szarowska, P. Newton, V. Dyachuk, L. Li, H. Qian, A. Johansson, Y. *Mishina, J. Currie, E. Tanaka, A. Erickson,* A. Dudley, H. Brismar, P. Southam, E. Coen, M. Chen, L. Weinstein, A. Hampl, E. Arenas, A. Chagin, K. Fried and I. Adameyko, *Oriented clonal cell dynamics enables accurate growth and shaping of vertebrate cartilage*, *eLife* **vol. 6,** (2017).

[21] M. Kaucka, J. Petersen, M. Tesarova, B. Szarowska, M. Kastriti, M. Xie, A. *Kicheva, K. Annusver, M. Kasper, O. Symmons, L. Pan,* F. *Spitz*, **J.** Kaiser, M. Hovorakova, T. Zikmund, K. Sunadome, M. Matise, H. Wang, U. Marklund, H. Abdo, P. Ernfors, P. Maire, M. Wurmser, A. Chagin, K. Fried and I. Adameyko, *Signals from the brain and olfactory epithelium control shaping of the mammalian nasal capsule cartilage*, *eLife* **vol. 7,** (2018).

[22] D. Noden and P. Trainor, Relations and interactions between cranial mesoderm and neural crest populations, Journal of Anatomy **vol.** ***207,*** *(2005).*

[23] B. de Boer, A. Soufan, J. Hagoort, T. Mohun, M. van den Hoff, A. Hasman, F. *Voorbraak, A. Moorman and J.* Ruijter, The interactive presentation of 3D information *obtained from reconstructed datasets and 3D placement of single histological sections with the 3D portable document format*, *Development* **vol. 138,** (2010).

[24] Congenital anomalies, Fact sheet No. 370, in World Health Organization, (2016).

[25] Birth defects: report by the Secretariat, Executive board 125th session EB125/7, in World Health Organization, (2009).

[26] A. Moon, Mouse Models for Investigating the Developmental Basis of Human Birth Defects, Pediatric Research **vol. 59**, (2006).

[27] M. Kaucka, *E. Ivashkin, D. Gyllborg, T. Zikmund, M. Tesarova, J. Kaiser*, M. Xie, J. Petersen, V. Pachnis, S. Nicolis, T. Yu, P. Sharpe, E. Arenas, H. Brismar, H. Blom, H. Clevers, U. Suter, A. Chagin, K. Fried, A. Hellander and I. Adameyko, *Analysis of neural crest–derived clones reveals novel aspects of facial development*, *Science Advances* **vol. 2,** (2016).

[28] C. Klingenberg, *Novelty and "Homology-free" Morphometrics: What's in a Name?,* Evolutionary *Biology* ***vol.*** **35**, (2008).

[29] D. Noden and P. Francis-West, The differentiation and morphogenesis of craniofacial muscles, Developmental Dynamics ***vol. 235**, (2006).*

[30] D. Suzuki, Y. Fukumoto, M. Yoshimura, Y. Yamazaki, J. Kosaka, S. Kuratani and H. Wada, Comparative morphology and development of extra-ocular muscles in the *lamprey and gnathostomes reveal the ancestral state and developmental patterns of the vertebrate* head*, Zoological* Letters **vol.** 2, (2016).

[31] G. Young, Number and arrangement of extraocular muscles in primitive gnathostomes: evidence from extinct placoderm fishes, Biology Letters **vol. 4**, (2007).

[32] P. Hasson, "Soft" tissue patterning: Muscles and tendons of the limb take their form, Developmental Dynamics **vol. 240**, (2011).

[33] A. Huang, Coordinated development of the limb musculoskeletal system: *Tendon and muscle patterning and integration with the skeleton, Developmental Biology* ***vol.*** **429**, *(2017).*

[34] G. Comai, M. Tesařová, V. *Dupé, M.* Rhinn*, P*. Vallecillo-García, F. da Silva, B. Feret, K. Exelby, P. Dollé, L. Carlsson, B. Pryce, F. Spitz, S. Stricker, T. Zikmund, J. Kaiser, J. Briscoe, A. Schedl, N. Ghyselinck, R. Schweitzer, S. Tajbakhsh and S. Hughes, *Local retinoic acid signaling directs emergence of the extraocular muscle functional unit*, *PLOS Biology* **vol. 18,** (2020).

[35] J. Porter, R. Baker, R. Ragusa and J. Brueckner, Extraocular muscles: Basic and clinical aspects of structure and function, Survey of Ophthalmology **vol.** ***39**, (1995).*

[36] E. Heude, *M. Tesarova, E. Sefton, E. Jullian, N. Adachi, A. Grimaldi, T.* Zikmund*, J.* Kaiser, G. Kardon, R. Kelly and S. Tajbakhsh, *Unique morphogenetic signatures define mammalian neck muscles and associated connective tissues*, *eLife* **vol. 7,** (2018).

[37] A. Emery, *The muscular dystrophies, Oxford University Press, New York,* ISBN 9780199542161 *(2001).*

[38] A. Martin, R. Reddy and M. Fehlings, Dropped head syndrome: diagnosis and management, Evidence-Based *Spine-Care Journal* ***vol. 2**, (2011).*

[39] M. Randolph and G. Pavlath, A muscle stem cell for every muscle: variability of satellite cell biology among different muscle groups, Frontiers in Aging Neuroscience **vol. 7**, (2015).

[40] R. Ericsson, R. Knight and Z. Johanson, Evolution and development of the vertebrate neck, Journal of Anatomy **vol. 222**, (2013*).*

[41] M. Tesařová, *Quantitative 3D characterization of biological structures by X-ray computed microtomography*, Doctoral thesis topic. Brno University of Technology, Central European Institute of Technology (2020).

7 Author publications and other outputs

7.1 Publications

First-author:

- **TESAŘOVÁ M.**; MANCINI L.; MAURI E.; ALJANČIČ G.; NAPARUS-ALJANČIČ M.; KOSTANJŠEK R.; MALI L.B.; ZIKMUND T.; KAUCKA M.; PAPI F.; GOYENS J.; BOUCHNITA A.; HELLANDER A.; ADAMEYKO I. and KAISER J. Living in darkness: Exploring adaptation of Proteus anguinus in 3D by X-ray imaging. *GigaScience*, 2022.
- **TESAŘOVÁ, M.**; HEUDE, E.; COMAI, G.; ZIKMUND, T.; KAUCKÁ, M.; ADAMEYKO, I.; TAJBAKHSH, S. and KAISER, J. An interactive and intuitive visualisation method for X-ray computed tomography data of biological samples in 3D Portable Document Format, *Scientific Reports*, 2019.
- **TESAŘOVÁ, M.**, MANCINI, L., SIMON, A., ADAMEYKO, I., KAUCKÁ, M., ELEWA, A., LANZAFAME, G., ZHANG, Y., KALASOVÁ, D., SZAROWSKÁ, B., ZIKMUND, T., NOVOTNÁ, M. and KAISER, J. A quantitative analysis of 3D-cell distribution in regenerating muscle-skeletal system with synchrotron X-ray computed microtomography, *Scientific Reports*, 2018.
- **TESAŘOVÁ, M.**; ZIKMUND, T.; KAUCKÁ, M.; ADAMEYKO, I.; JAROŠ, J.; PALOUŠEK, D.; ŠKAROUPKA, D. and KAISER, J. Use of micro computed- tomography and 3D printing for reverse engineering of mouse embryo nasal capsule. *Journal of Instrumentation*, 2016.

Co-author:

- KAMENEVA P.; MELNIKOVA V.; KASTRITI M.E.; KURTOVA A.; KRYUKOV E.; MURTAZINA A.; FAURE L.; POVERENNAYA I.; ARTEMOV A.; KALININA T.; KUDRYASHOV N.; BADER M.; SKODA J.; CHLAPEK P.; CURYLOVA L.; SOURADA L. NERADIL J.; **TESAŘOVÁ M.**; GASPAR P.; YAKUSHOV V.D.; SHEFTEL B.I.; ZIKMUND T.; KAISER J.; FRIED K. ALENINA N.; VORONEZSHKAYA E. and ADAMEYKO I. Serotonin limits generation of chromaffin cells during adrenal organ development. *Nature Communications*, 2022.
- MATULA J.; POLAKOVA V.; SALPLACHTA J.; **TESAŘOVÁ M**.; ZIKMUND T.; KAUCKÁ M.; ADAMEYKO I. and KAISER J. Resolving complex cartilage structures in developmental biology via deep learning-based automatic segmentation of X-ray computed microtomography images. *Scientific Reports*, 2022.
- BOUDERLIQUE T.; PETERSEN J.; FAURE L. ABED-NAVANDI D.; BOUCHNITA A.; MUELLER B.; NAZAROV M.; ENGLMAIER L.; **TESAŘOVÁ M.**; FRADE P.R.; ZIKMUND T.; KOEHNE T.; KAISER J. FRIED K.; WILD C.; PANTOS O.; HELLANDER A.; BYTHELL J. and ADAMEKO I. Surface flow for colonial integration in reef-building corals. *Current Biology*, 2022.
- MATULA, J.; **TESAŘOVÁ, M.**; ZIKMUND, T.; KAUCKÁ, M.; ADAMEYKO, I. and KAISER, J. X-ray microtomography–based atlas of mouse cranial development. *GigaScience*, 2021.
- COMAI, G.; **TESAŘOVÁ, M.**; DUPÉ, V.; RHINN, M.; VALLECILLO-GARCÍA, P.; DA SILVA, F.; FERET, B.; EXELBY, K.; DOLLE, P.; CARLSSON, L.; PRYCE, B.; SPITZ, F.; STRICKER, S.; ZIKMUND, T.; KAISER, J.; BRISCOE, J.; SCHEDL, A.; GHYSELINCK, N.; SCHWEITZER, R. and TAJBAKHSH, S. Local retinoic acid signaling directs emergence of the extraocular muscle functional unit. *PLOS Biology*, 2020.
- HEUDE, E.; **TESAŘOVÁ, M.**; SEFTON, E. M.; JULLIAN, E.; ADACHI, N.; GRIMALDI, A.; ZIKMUND, T.; KAISER, J.; KARDON, G.; KELLY, R. G. and TAJBAKHSH, S. Unique morphogenetic signatures define mammalian neck muscles and associated connective tissues. *eLife*, 2018.

- KAUCKA, M.; PETERSEN, J.; **TESAŘOVÁ, M.**; SZAROWSKA, B.; KASTRITI, ME.; XIE, M.; KICHEVA, A.; ANNUSVER, K.; PAN, L.; SPITZ, F.; KAISER, J.; HOVORAKOVA, M.; ZIKMUND, T.; SUNADOME, K.; MATISE, MP.; WANG, H.; MARKLUND, U.; ABDO, H.; ERNFORS, P.; MAIRE, P.; WURMSER, M.; CHAGIN, AS.; FRIED, K. and ADAMEYKO, I. Signals from the brain and olfactory epithelium control shaping of the mammalian nasal capsule cartilage. *eLife*, 2018.
- ZIKMUND, T.; NOVOTNÁ, M.; KAVKOVÁ, M.; **TESAŘOVÁ, M.**; KAUCKÁ, M.; SZAROWSKÁ, B.; ADAMEYKO, I.; HRUBÁ, E.; BUCHTOVÁ, M.; DRAŽANOVÁ, E.; STARČUK, Z. and KAISER, J. et al. High-contrast differentiation resolution 3D imaging of rodent brain by X-ray computed microtomography. *Journal of Instrumentation*, 2018.
- KAUCKÁ, M.; ZIKMUND, T.; **TESAŘOVÁ, M.**; GYLLBORG, D.; HELLANDER, A.; JAROŠ, J.; KAISER, J.; PETERSEN, J.; SZAROWSKA, B.; NEWTON, P.T.; DYACHUK, V.; LI, L.; QIAN, H.; JOHANSSON, A-S.; MISHINA, Y.; CURRIE, J.; TANAKA, E.M.; ERICKSON, A.; DUDLEY, A.; BRISMAR, H.; SOUTHAM, P.; COEN, E.; CHEN, M.; WEINSTEIN, L.S.; HAMPL, A.; ARENAS, E.; CHAGIN, A.S.; FRIED, K. and ADAMEYKO, I. Oriented clonal cell dynamics enables accurate growth and shaping of vertebrate cartilage. *eLife*, 2017.
- JAROŠ, J.; PETROV, M.; **TESAŘOVÁ, M**. and HAMPL, A. Revealing 3D Ultrastructure and Morphology of Stem Cell Spheroids by Electron Microscopy. *Methods Molecular Biology*, 2017.
- KAUCKÁ, M.; IVASHKIN E.; GYLBORG, D.; ZIKMUND, T.; **TESAŘOVÁ, M.**; KAISER, J.; XIE, M.; PETERSEN, J.; PACHNIS, V.; NICLOIS, S.K.; YU, T.; SHARPE, P.; ARENAS, E.; BRISMAR, H.; BLOM, H.; CLEVERS, H.; SUTER, U.; CHAGIN, A.S.; FRIED, K.; HELLANDER, A. and ADAMEYKO, I. Analysis of neural crest- derived clones reveals novel aspects of facial development. *Science Advances*, 2016.

Submitted publications:

- KAUCKA M.; JOVEN A.; **TESAŘOVÁ M.**; CURRIE J.; PETERSEN J.; YAO Z.; BOUCHNITA A.; HELLANDER A.; ZIKMUND T.; ELEWA A.; NEWTON P.; FEI J.F.; CHAGIN A.; FRIED K.; TANAKA E. KAISER J.; SIMON A. AND ADAMEYKO I. Limb regeneration in salamanders leads to bulky long bones through variations of developmental programs. *Nature Communications*, 2022 (*awaiting resubmission*).
- SUNADOME K.; ERICKSON A.; KAH D.; FABRY B.; ADORI C.; KAMENEVA P.; FAURE L.; KANATANI S.; KAUCKA M.; DEHNISCH I.; **TESAŘOVÁ M.**; ZIKMUND T.; KAISER J.; EDWARDS S.; MAKI K.; ADACHI T.; FRIED K. and ADAMEYKO I. Directionality of developing skeletal muscles is set by mechanical forces. *Nature Communications*, 2022 (*under review*).
- PETERSEN J.; ENGLMAIER L.; ARTEMOV A.; POVERENNAYA I.; BOUDERLIQUE T.; **TESAŘOVÁ M**.; DEVIATIIAROV R.; SZILVASY-SZABO A.; AKKURATOV E.; ZEBERG H.; KAUCKA M.; KASTRITI M.E.; KRIVANEK J.; RADASZKIEWICZ T.; GRABOWSKI A. ZIKMUND T.; KAVKOVÁ M.; AXELSON H.; LINDGREN D.; KRAMANN R.; KUPPE C.; ERDÉLYI F.; MÁTÉ Z.; SZABO G.; KOEHNE T.; BRYJA V.; HARKANY T.; FRIED K.; KAISER J.; CSABA F.; GUSEV O. and ADAMEYKO I. A previously uncharacterized Kidney-Associated Membrane Protein (KAMP) is associated with evolutionary adaptation, energy balance and kidney physiology. *Nautre Communications*, 2022 (*awaiting resubmission*).

7.2 Products

- ŠALPLACHTA, J.; **TESAŘOVÁ, M.**; ZEMEK, M. and KAISER, J.: Sample holder with a reference area (functional sample). Output of TAČR ZÉTA TJ02000127

7.3 Grants

- Bridge fund 2021-2022: “3D characterization of lymphotic leukemia cells´migration by X-ray computed microtomography” – Cooperation between CEITEC research groups Advanced Instrumentation and Methods for Materials Characterization (Tomáš Zikmund) and Microenvironment of Immune Cells (Marek Mráz).
- TAČR ZÉTA – “Differentiation of soft tissues by dual-target tomography” - TJ02000127 (5/2019-4/2021) – main applicant. Cooperation between Brno University of Technology and Rigaku Innovative Technologies Europe s.r.o
- Martina Roeselova memorial fellowship 2020.
- BUT Internal projects – main applicant
    - “Shaping of skeletal elements during regeneration of salamander limbs by X-ray computed microtomography” - CEITEC VUT-J-21-7145 (2021).
    - “Morphogenesis of the extraocular muscles in 3D by X-ray computed microtomography” – CEITEC VUT-J-20-6317 (2020).
    - “Application of industrial X-ray computed tomography for muscle-skeletal imaging at vertebrates” – CEITEC VUT-J-19-5764 (2019).
- Brno PhD Talent 2018.
- AFM Telethon 21853 – “Investigating heterogeneities and morphogenesis of cranial mesoderm derived skeletal muscles” (2017-2018).

7.4 Conferences

May 2022	4th International meeting SOS Proteus: Conservation of Proteus and its habitat facing climate change challenge, Trieste, Italy *Oral presentation*: 3D exploring of *Proteus anguinus* by X-ray computed microtomography
October 2021	35th Conference of Czech Herpetological Society, Prague, Czech Republic *Oral presentation*: Rentgenová počítačová mikrotomografie jako nástroj ke studiu (nejen) macaráta jeskynního (in Czech language)
September 2021	Conference of The Visegrád Group Society for Developmental Biology (V4SDB), Szeged, Hungary *Oral presentation*: Revealing secrets of *Proteus anguinus* by 3D X-ray imaging
June 2019	Joint Retreat, Kouty u Ledče nad Sázavou, Czech Republic *Oral presentation*: Application of industrial X-ray computed tomography for muscle-skeletal imaging at vertebrates
July 2018	International symposium on morphological sciences, Prague, Czech Republic *Oral presentation*: Implementation of industrial approach of X-ray computed microtomography in developmental biology.
June 2018	European Workshop on laser ablation, Pau France

	Poster: Combination of Laser-Induced Breakdown Spectroscopy and Computed Tomography for 3D chemical imaging.
September 2017	International workshop on Imaging, Varenna, Italy *Poster*: Quantitative 3D analysis at cellular resolution with X-ray computed microtomography.
April 2017	Bioimplantology, Brno, Czech Republic *Oral presentation*: Application of X-ray Computed Tomography for 3D imaging with cellular resolution.